TU Delft

Delft University of Technology

Document Version
Final published version

Licence
CC BY

Citation (APA)
Jakob, M., Laubscher, K., Del Vecchio, P., Chatterjee, A., Fatemi, V., & Bosco, S. (2026). Fast readout of quantum dot spin qubits via Andreev spins. *Physical Review Applied*, *26*(3), Article 034009. https://doi.org/10.1103/qcch-2hhy

Important note
To cite this publication, please use the final published version (if applicable).
Please check the document version above.

Copyright
In case the licence states “Dutch Copyright Act (Article 25fa)”, this publication was made available Green Open Access via the TU Delft Institutional Repository pursuant to Dutch Copyright Act (Article 25fa, the Taverne amendment). This provision does not affect copyright ownership.
Unless copyright is transferred by contract or statute, it remains with the copyright holder.

Sharing and reuse
Other than for strictly personal use, it is not permitted to download, forward or distribute the text or part of it, without the consent of the author(s) and/or copyright holder(s), unless the work is under an open content license such as Creative Commons.

Takedown policy
Please contact us and provide details if you believe this document breaches copyrights.
We will remove access to the work immediately and investigate your claim.

This work is downloaded from Delft University of Technology.

Fast readout of quantum dot spin qubits via Andreev spins

Michèle Jakob,[1,*] Katharina Laubscher,[2,*] Patrick Del Vecchio,[1] Anasua Chatterjee,[1] Valla Fatemi,[3] and Stefano Bosco[1,†]

[1]*QuTech and Kavli Institute of Nanoscience, Delft University of Technology, Delft, The Netherlands*
[2]*Condensed Matter Theory Center and Joint Quantum Institute, Department of Physics, University of Maryland, College Park, Maryland 20742, USA*
[3]*School of Applied and Engineering Physics, Cornell University, Ithaca, New York, 14853, USA*

(Received 22 July 2025; revised 11 June 2026; accepted 5 August 2026; published 3 September 2026)

Spin qubits in semiconducting quantum dots are currently limited by slow readout processes, which are orders of magnitude slower than gate operations. In contrast, Andreev spin qubits benefit from fast measurement schemes enabled by the large resonator couplings of superconducting qubits but suffer from reduced coherence during qubit operations. Here, we propose fast and high-fidelity measurement protocols based on an electrically tunable coupling between quantum dot and Andreev spin qubits. In realistic devices, this coupling can be made sufficiently strong to enable high-fidelity readout well below microseconds, potentially enabling mid-circuit measurements. Crucially, the electrical tunability of our coupler permits to switch it off during idle periods, minimizing crosstalk and measurement back-action. Our approach is fully compatible with germanium-based devices and paves the way for scalable quantum computing architectures by leveraging the advantages of heterogeneous qubit implementations.

DOI: 10.1103/qcch-2hhy

I. INTRODUCTION

Quantum dot spin qubits (DSQs) [1], especially those based on silicon and germanium (Ge) heterostructures [2,3], are leading candidates for large-scale quantum computing [4]. These systems combine a compact footprint and compatibility with industrial semiconductor fabrication processes with high quantum performance [5–20]. DSQs exhibit long coherence times and support high-fidelity single- and two-qubit gate operations, often exceeding fault-tolerance thresholds [21–24], with gate times of tens of nanoseconds [25–31] and operation demonstrated in mid-scale devices [32–35]. Despite these advantages, a key challenge in DSQ systems remains the readout, which is significantly slower than gate operations because of small DSQ-readout channel couplings [36]. State-of-the-art devices require integration times typically of tens to hundreds of microseconds, to reach high-fidelity spin readout [4,37–42]. This readout bottleneck introduces idling errors and poses serious limitations for quantum error correction protocols and algorithms requiring frequent measurements.

In contrast, Andreev spin qubits (ASQs) comprising spins localized in semiconductors proximitized by superconducting Josephson junctions [43–53] benefit from strong inductive coupling to on-chip microwave resonators, enabling high-fidelity readout within hundreds of nanoseconds [45,52] and long-range connectivity [48]. Ge heterostructures are particularly promising for ASQs [54,55]. Their compatibility with superconductors [56–61] has recently enabled significant proximity-induced superconducting gaps [54,62–64] and demonstrations of gate-tuneable Josephson junctions [65,66]. The potential for isotopic purification [67] and p-type wavefunction [68–70] of Ge can suppress nuclear spin noise, likely a key limiting factor of current ASQs [46,47]. Furthermore, the strong, tunable spin-orbit interaction (SOI) in hole nanostructures, especially large in lattice-matched unstrained [71–73] and tensile-strained [74–76] Ge channels, offers efficient electrical control of the qubit. These properties make Ge an ideal platform for hybrid superconducting-semiconducting spin qubit architectures [77–79].

Here, we propose a tunable coupling scheme between DSQs and ASQs, see Fig. 1, combining the high-fidelity gate operations of DSQs with the fast, efficient readout capability of ASQs. The coupling is electrically switched: it remains off during DSQ gate operations to suppress crosstalk and back-action [80–82] and is activated only during the readout phase. We present several readout

*These authors contributed equally to this work.
†Contact author: s.bosco@tudelft.nl

Published by the American Physical Society under the terms of the Creative Commons Attribution 4.0 International license. Further distribution of this work must maintain attribution to the author(s) and the published article's title, journal citation, and DOI.

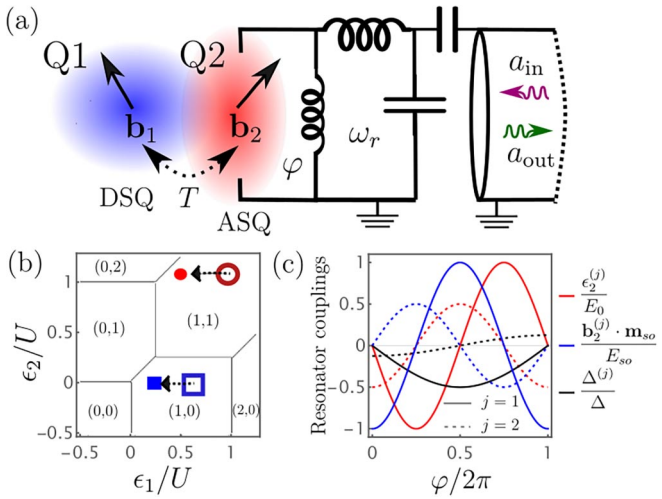

FIG. 1. Tuneable ASQ-DSQ coupler. (a) A DSQ (Q1) is tunnel-coupled to an ASQ (Q2), inductively coupled to a microwave resonator. (b) Charge stability diagrams for $U_{11} = U_{22} = 4U_{12} \equiv U$ at $T = \Delta = 0$, see Eqs. (A1) and (2). Filled blue and red dots represent two fast-readout points with large ASQ-DSQ hybridization when Q2 is empty and occupied, respectively. The hybridization is suppressed electrically by decreasing T or modifying the Q1-Q2 detuning by moving toward the hollow dots, where high-fidelity quantum gates on DSQs can be performed without back-action from the ASQ. (c) Amplitude of the inductive resonator-ASQ interactions against φ, see Eq. (B2).

protocols tailored to different experimental configurations, all compatible with Ge-based hybrid devices [54,65]. Our analysis indicates that readout fidelities beyond 99.9% can be achieved well below microseconds, representing orders-of-magnitude improvements in measurement speed. We envision that by leveraging strong inductive ASQ-resonator coupling, which enables long-range ASQ-ASQ connectivity [83,84], our ASQ-DSQ coupler could also mediate entangling gates of distant DSQs, overcoming their short-range connectivity limitations [85] and offering opportunities for flexible layouts in large-scale spin-based quantum processors.

II. TUNABLE ASQ-DSQ COUPLER

We consider two quantum dots, where dot $i = 1$ hosts a DSQ and dot $i = 2$ is proximitized by two superconducting leads with phase difference φ and forms an ASQ, see Fig. 1(a). The coupled DSQ-ASQ system is described by the Hamiltonian

$$H_0 = \sum_i \mathbf{c}_i^\dagger h_i \mathbf{c}_i - \Delta_\varphi (c_{2\uparrow}^\dagger c_{2\downarrow}^\dagger + c_{2\downarrow} c_{2\uparrow}) + \sum_{ij,\sigma\sigma'} \frac{U_{ij}}{2} n_{i\sigma} n_{j\sigma'}, \tag{1}$$

where $\mathbf{c}_i = (c_{i\uparrow}, c_{i\downarrow})$ are fermion operators with density $n_{i\sigma} = c_{i\sigma}^\dagger c_{i\sigma}$, see the Appendixes for more details. The Hubbard intradot and interdot interactions U_{ii} and $U_{12} = U_{21}$, respectively, satisfy $U_{12}^2 < U_{11}U_{22}$ [86] and define the charge stability diagrams sketched in Fig. 1(b). The single-particle Hamiltonian of dot i, $h_i = -(\epsilon_i + 2U_{ii})\sigma_0 + \mathbf{b}_i \cdot \boldsymbol{\sigma}/2$, includes dot energies ϵ_i, Zeeman energies $\mathbf{b}_i$, and a shift $2U_{ii}$ that cancels the $n_{i\sigma}^2 = n_{i\sigma}$ contributions of the Hubbard energy. For the DSQ, the dot energy coincides with its chemical potential, $\epsilon_1 = \mu_1$, and the Zeeman energy $\mathbf{b}_1 = \mu_B \mathbf{B} g_1$ is determined by the magnetic field $\mathbf{B}$ and the tuneable dot g-tensor [72,87–90]. For the ASQ, $\epsilon_2 = \mu_2 + E_0 \cos\varphi$ depends on φ via the Josephson energy E_0. The Zeeman energy $\mathbf{b}_2 = \mu_B \mathbf{B} g_2 - E_{so} \sin(\varphi) \mathbf{m}_{so}$ also includes the additional phase-dependent SOI-contribution E_{so} [43,49,50] aligned to the SOI vector $\mathbf{m}_{so}$. The ASQ also inherits from the superconducting leads the proximitized correlations $\Delta_\varphi = \Delta \cos(\varphi/2)$ [91–94]. While Eq. (A1) was derived under the assumption that the parent gap in the superconducting leads is much larger than the charging energy of the dots, numerical studies have shown that H_0 remains qualitatively valid well beyond the large-gap limit [49]. Additional information on the small-gap limit is provided in the Appendixes.

Crucially, DSQ and ASQ are coupled by the tunneling $T/h \in [1\text{–}10]$GHz. Gate potentials efficiently control T on-demand [27], turning it on only during readout. The interaction

$$H_T = -T[\mathbf{c}_1^\dagger \tilde{S}_{so} \mathbf{c}_2 + \mathbf{c}_2^\dagger \tilde{S}_{so}^\dagger \mathbf{c}_1] \tag{2}$$

includes the SOI-induced spin-flip unitary evolution $\tilde{S}_{so} = e^{i\tilde{\theta}_{so} \tilde{\mathbf{n}}_{so} \cdot \boldsymbol{\sigma}/2}$, characterized by a rotation angle $\tilde{\theta}_{so}$ around the SOI axis $\tilde{\mathbf{n}}_{so}$, generally not aligned to $\mathbf{m}_{so}$.

In unstrained Ge channels where SOI is maximized [71–73], we expect $E_{so}/h \in [10\text{–}500]$ MHz, $E_0/h \in [0.3\text{–}1]$ GHz, and $\Delta/h \in [4\text{–}10]$ GHz, see the Appendixes for details. These values are comparable to existing InAs-based ASQs [46,49]. Our estimate for Δ is based on recently realized Ge/PtSiGe devices [62]; however, significantly larger gaps can in principle be achieved in Ge-based devices proximitized by Al or Nb [63]. For in-plane magnetic fields up to 200 mT, within the critical field of Ge-compatible superconductors [54,62,63], $\mathbf{b}_i/h \in [0.1\text{–}1]$ GHz [27,32], with controllable direction and amplitude by dot and strain engineering [72,87].

III. INDUCTIVE COUPLING TO RESONATOR

Our readout is performed by an inductively coupled resonator with energy $\hbar\omega_r a^\dagger a$. Inductive coupling shifts the phase $\varphi \to \varphi + X\varphi_r$, where $X = (a^\dagger + a)/\sqrt{2}$. The effective zero-point-phase $\varphi_r = p\sqrt{2\pi Z_r/R_q} \in [0.02\text{–}1]$ depends on the resonator impedance $Z_r \in [0.05\text{–}1]$ $k\Omega$, the superconducting resistance quantum $R_q = h/4e^2$ [95], and is rescaled by the participation ratio $p \in [0.1\text{–}1]$ accounting for the partial fraction of the resonator phase

reaching the ASQ. At $Z_r = 300\,\Omega$ and $p = 0.3$, $\varphi_r = 0.16$. We restrict to low-impedance resonators ($Z_r \ll 1\ k\Omega$), in contrast to capacitively coupled systems [96–104] where high-impedance resonators are required to enhance spin-photon coupling at the cost of losses and complexity.

The coupling Hamiltonian

$$H_I = \sum_{j>0} \varphi_r^j X^j \left(\mathbf{c}_2^\dagger \frac{\mathbf{b}_2^{(j)} \cdot \boldsymbol{\sigma} - 2\epsilon_2^{(j)}}{2} \mathbf{c}_2 - \Delta^{(j)} c_{2\uparrow}^\dagger c_{2\downarrow}^\dagger + \text{H.c.} \right) \tag{3}$$

includes resonator-induced fluctuations of ASQ dot and Zeeman energy, $\epsilon_2^{(j)} = \partial_\varphi^j \epsilon_2 / j \propto E_0$ and $\mathbf{b}_2^{(j)} = \partial_\varphi^j \mathbf{b}_2 / j \propto E_{so} \mathbf{m}_{so}$, respectively, and the resonator-mediated pairing $\Delta^{(j)} = \partial_\varphi^j \Delta_\varphi / j \propto \Delta$. The first- and second-order susceptibilities are shown in Fig. 1(c). The spin-independent terms $\epsilon_2^{(j)}$ and $\Delta^{(j)}$ are odd (even) functions of φ at $j = 1$ ($j = 2$), while $\mathbf{b}_2^{(j)}$ has the opposite parity.

IV. SINGLE-PARTICLE REGIME

We consider a single particle confined in our hybrid double dot, a stable configuration because of U_{ij}, see Fig. 1(b). To minimize crosstalk and ASQ-mediated noise, we assume DSQ quantum gates are performed in the (1,0) region (hollow blue square) and ASQ-DSQ hybridization is activated only during readout by increasing T and moving closer to the (0,1) region (solid blue square). Possible detrimental effects of residual tunnelings and interdot interactions during DSQ operation can be suppressed by adding an empty dot between the DSQ and ASQ, and coherently shuttling the DSQ [105] to the empty dot during readout.

From Eqs. (A1) and (2) and using third-order perturbation theory, we find the hopping Hamiltonian

$$H_{1\text{P}} = -\tau_z \frac{\epsilon_\varphi}{2} + \tau_1 \frac{b_1 \sigma_z}{2} + \tau_2 \frac{b_2 \sigma_z}{2} - T_\varphi (\tau_+ S_{so} + \tau_- S_{so}^\dagger), \tag{4}$$

where the Pauli matrices τ act on the dot subspace, $\tau_\pm = (\tau_x \pm i\tau_y)/2$ and $\tau_{1,2} = (\tau_0 \pm \tau_z)/2$. We aligned both Zeeman fields to the z-direction by a local spin-rotation R_i generated by $\tau_i U_i = \tau_i e^{-i\Theta_i \mathbf{n}_i \cdot \boldsymbol{\sigma}/2}$, that satisfies $U_i^\dagger (\mathbf{b}_i \cdot \boldsymbol{\sigma}) U_i = (R_i \mathbf{b}_i) \cdot \boldsymbol{\sigma} = b_i \sigma_z$. In this frame, the spin-flip tunneling operator transforms as $S_{so} = U_1^\dagger \tilde{S}_{so} U_2 \equiv e^{i\theta_{so} \mathbf{n}_{so} \cdot \boldsymbol{\sigma}/2}$, with modified θ_{so} and $\mathbf{n}_{so}$.

The correlations Δ_φ renormalize dot detuning $\epsilon_\varphi \approx \epsilon + \Delta_\varphi^2 / \mathcal{U}$ and tunneling $T_\varphi = T[1 - \Delta_\varphi^2/(2\mathcal{U}(\mathcal{U} - \epsilon))]$, adding a φ dependence to T. Here, $\epsilon = \epsilon_1 - \epsilon_2$ and $\mathcal{U} = U_2 + 2U_{12} - 2\epsilon_2$. Finally, the unitary U_2 diagonalizing $\mathbf{b}_2 \cdot \boldsymbol{\sigma}$ generally depends on φ and imprints a φ-dependence to S_{so}. We envision that this could enable efficient ASQ-DSQ interactions engineering by biasing φ, also mediating additional resonator couplings that we neglect here.

V. HYBRIDIZED DSQ

The hopping Hamiltonian $H_{1\text{P}}$ in Eq. (B3) enables different readout schemes. A possible protocol involves physically transferring the spin from the DSQ to the ASQ, e.g., by activating T while decreasing ϵ, and then reading out the ASQ spin via its large direct inductive coupling $\mathbf{b}_2^{(2)}$ to the resonator [52].

While experimental advances in shuttling DSQs make this approach promising [27,105], here we consider the case where the spin remains confined in the DSQ and hybridizes to the ASQ by $T_\varphi \lesssim \epsilon_\varphi$, in analogy to flopping-mode qubits [106,107]. The ASQ modifies the DSQ's Zeeman energy as

$$H_{hy} = \frac{(1-\eta) b_1 \sigma_z}{2} + \eta \frac{b_2 (R_{so} \mathbf{e}_z) \cdot \boldsymbol{\sigma}}{2}, \tag{5}$$

where $S_{so} \sigma_z S_{so}^\dagger = (R_{so} \mathbf{e}_z) \cdot \boldsymbol{\sigma}$ includes tilting of g-tensors and spin-flip tunneling.

The DSQ-ASQ hybridization is captured by $\eta = 1/2 - \epsilon_\varphi / 2E_g \approx T_\varphi^2 / \epsilon_\varphi^2$, where $E_g = \sqrt{4T_\varphi^2 + \epsilon_\varphi^2}$ is the orbital energy and mediates the DSQ-resonator coupling $H_{hy,I} = (\varphi_r X \boldsymbol{\gamma}^{(1)} + \varphi_r^2 X^2 \boldsymbol{\gamma}^{(2)}) \cdot \boldsymbol{\sigma}$, where

$$\boldsymbol{\gamma}^{(1)} \approx \eta \frac{R_{so} \mathbf{b}_2^{(1)}}{2} - \eta^{(1)} \frac{b_1 - b_2 R_{so}}{2} \mathbf{e}_z, \tag{6a}$$

$$\boldsymbol{\gamma}^{(2)} \approx \eta \frac{R_{so} \mathbf{b}_2^{(2)}}{2} - \eta^{(2)} \frac{b_1 - b_2 R_{so}}{2} \mathbf{e}_z + \frac{\eta^{(1)} R_{so} \mathbf{b}_2^{(1)}}{2}. \tag{6b}$$

The vectors $\boldsymbol{\gamma}^{(j)}$ comprise two distinct contributions: the magnetic susceptibility of the ASQ $\mathbf{b}_2^{(j)} = \partial_\varphi^j \mathbf{b}_2 / j$ and the orbital susceptibility $\eta^{(j)} = \partial_\varphi^j \eta / j$. These have a complementary φ dependence, opposite for $\boldsymbol{\gamma}^{(1)}$ and $\boldsymbol{\gamma}^{(2)}$, as shown in Figs. 2(a) and 2(b), enabling the selective utilization of different couplings by flux biasing.

VI. READOUT FIDELITY

The DSQ-resonator interaction enables an efficient discrimination of spin up and down states. The readout is performed by driving the resonator via a weakly coupled input field $a_{\text{in}} = A e^{-i\omega t} / \sqrt{\kappa}$ with amplitude A and coupling rate κ, yielding the driving Hamiltonian $H_d^R = \sqrt{2} A X$ in the frame rotating at the driving frequency $\omega = \omega_r$. In this frame, to second order in φ_r, the DSQ-resonator interaction Hamiltonian produces the spin-dependent ac Stark shift

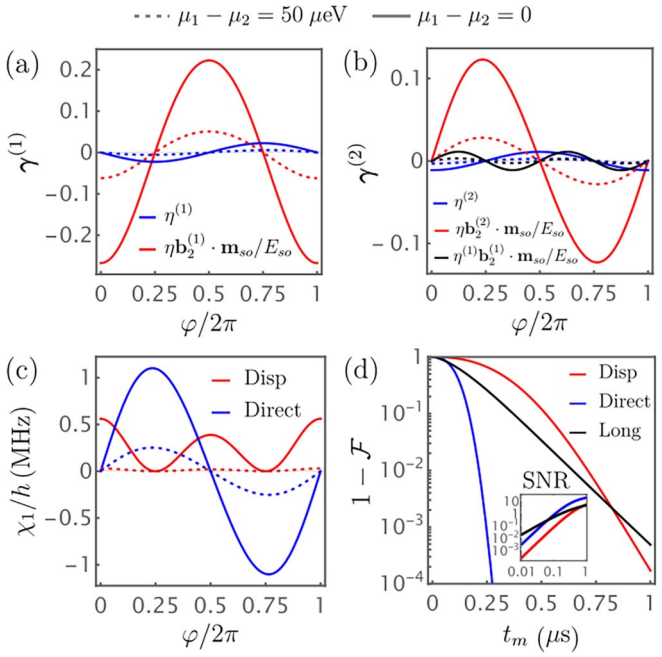

FIG. 2. Hybrid DSQ readout. (a),(b) Amplitude of the (a) first- and (b) second-order DSQ-resonator couplings $\boldsymbol{\gamma}^{(j)}$ [see Eq. (6)] against φ for different dot detunings. We use $\Delta/h = 8$ GHz, $E_{so}/h = 0.35$ GHz, and $E_0/h = 0.9$ GHz reachable in unstrained Ge. Also, $\varphi_r = 0.16$, $\mu_1 = 0.2$ meV, $T/h = 5$ GHz, and $U_{11} = U_{22} = 4U_{12} = 1$ meV. (c) Dispersive and direct resonator shifts [see Eq. (7)]. We assume the optimal scenario for each coupling with $\boldsymbol{\gamma}^{(1)} \perp \mathbf{e}_z$ and $\boldsymbol{\gamma}^{(2)} \| \mathbf{e}_z$, respectively. (d) Readout infidelity in logarithmic scale of frequency-modulated and longitudinal readout schemes. Inset: SNR against t_m in double-logarithmic scale. We use $\chi_1/\hbar = \kappa/2 = 2\pi \times 0.56$ MHz (1.1 MHz), $A = \kappa\sqrt{\bar{n}/2}$, with $\bar{n} = 2$ ($\bar{n} = 10$) and $|\hbar\omega_r - b_{hy}|/h = 0.2$ GHz for dispersive (direct) readout. For longitudinal readout, by modulating $T = T_0 + \delta T \cos(\omega_r t)$ with $T_0/h = 2\delta T/h = 5$ GHz at $\mu_2 - \mu_1 = 50$ μeV, $\varphi = 0$, and $\boldsymbol{\gamma}^{(1)} \| \mathbf{e}_z$, we estimate $\delta\eta \approx \delta T \partial_T \eta \approx 0.06$ and $g_z/h \approx 1.26$ MHz.

$$H^R_{hy,I} = \chi_1 a^\dagger a \sigma_z, \quad \text{with}$$
$$\chi_1 \approx \frac{\varphi_r^2 |\boldsymbol{\gamma}^{(1)} \times \mathbf{e}_z|^2}{2(b_{hy} - \hbar\omega_r)} + \varphi_r^2 \boldsymbol{\gamma}^{(2)} \cdot \mathbf{e}_z. \tag{7}$$

This includes a dispersive [95] and direct inductive coupling [52], dependent on $\boldsymbol{\gamma}^{(1)} \times \mathbf{e}_z$ and $\boldsymbol{\gamma}^{(2)} \cdot \mathbf{e}_z$, respectively. We neglect the Lamb shift modifying the DSQ frequency and introduce the Zeeman field amplitude $b_{hy} = |[(1-\eta)b_1 + \eta b_2 R_{so}] \cdot \mathbf{e}_z|$, see Eq. (5).

Importantly, these contributions are complementary in two ways. Comparing to Fig. 2(c), their flux dependence is opposite: at $\varphi = 0$, the dispersive and direct couplings are maximal and minimal, respectively, and at $\varphi = \pi/2$, the situation is inverted. We expect $\chi_1/h \sim 1$ MHz, comparable to superconducting qubits [95], enabling fast readout. Moreover, they show complementary trends depending on the direction of $\boldsymbol{\gamma}$ relative to the Zeeman field: dispersive and direct couplings depend on the transversal and longitudinal components of $\boldsymbol{\gamma}^{(j)}$, respectively. Because the angle $\boldsymbol{\gamma}^{(j)} \cdot \mathbf{e}_z$ can be engineered, e.g., by aligning $\mathbf{B}$ to the SOI [102,108] or by electrically tuning g-tensors [32,109], we compare optimal scenarios with $\boldsymbol{\gamma}^{(1)} \perp \mathbf{e}_z$ and $\boldsymbol{\gamma}^{(2)} \| \mathbf{e}_z$.

Similar to superconducting qubits, χ_1 imprints a spin dependence to the output field a_{out} integrated for a time t_m, which enables readout of the DSQ with signal-to-noise ratio [95,110]

$$\text{SNR} = |A| \sqrt{\frac{8t_m}{\kappa}} \left[1 - \frac{2}{\kappa t_m} \left(1 - e^{-\frac{\kappa t_m}{2}} \cos\left(\frac{\kappa t_m}{2} \right) \right) \right], \tag{8}$$

where we use the maximal steady-state SNR condition $\chi_1/\hbar = \kappa/2$ [111]. Small SNR causes errors in discriminating the state that leads to the readout infidelity $1 - \mathcal{F} = \text{erfc}(\text{SNR}/2)$ [112,113]. Here, we neglect reductions in fidelity coming from limited readout chain efficiency [114] that can be suppressed, e.g., by optimized filtering and pulse shaping [115–117]. Also, projective readout can be degraded by finite relaxation times T_1, whose effect on fidelity is discussed in the Appendixes.

In Fig. 2(d), we show that our hybrid DSQ-ASQ system enables high-fidelity readout below microseconds for dispersive and direct couplings (red and blue curves, respectively). In the setup considered, the direct coupling (blue curve) enables faster readout, see Fig. 2(c). This is not only because of its larger χ_1, but also because the direct coupling is independent of the resonator-qubit detuning $|\hbar\omega_r - b_{hy}|$, and we operate the setup at larger resonator frequencies ω_r. This permits us to relax stringent conditions imposed by the dispersive regime on the maximal driving amplitudes $A \ll A_{\text{crit}} = \kappa\sqrt{\bar{n}_{\text{crit}}/2}$, with critical photon number $\bar{n}_{\text{crit}} = |\hbar\omega_r - b_{hy}|/4\chi_1 \approx 25$ [81,113] at 0.2 GHz detuning and 2 MHz dispersive shift, and suppresses thermal photons and qubit-induced resonator nonlinearities [118,119].

Finally, the large first-order longitudinal component of $\boldsymbol{\gamma}^{(1)} \cdot \mathbf{e}_z$, complemented by a harmonic modulation of $\eta \to \eta_0 + \delta\eta \cos(\omega_r t)$ obtained by driving T, ϵ, or φ, produces the parametric longitudinal coupling $g_z \cos(\omega_r t)(a^\dagger + a)\sigma_z$, with $g_z \approx \varphi_r \delta\eta \mathbf{e}_z \cdot R_{so} \mathbf{b}_2^{(1)}/2\sqrt{2}$. We estimate that by modulating T, g_z/h can reach the MHz range also when the DSQ and ASQ are detuned. This coupling enables an efficient readout [110,120] in the short-time limit with $\text{SNR}_z = |g_z|\sqrt{8t_m/\kappa}[1 - 2(1 - e^{-\kappa t_m/2})/\kappa t_m]$, see black lines in Fig. 2(d), offering another fast DSQ-readout option.

VII. TWO-PARTICLE REGIME

We also examine the (1,1) sector of the charge stability diagram where two particles are confined in the double

dot, see red dots of Fig. 1(b). Filled (hollow) dots represent readout (operational) regions, where the DSQ and ASQ are coupled (decoupled). Fourth-order perturbation theory of Eqs. (A1) and (2) results in the exchange-coupled spin Hamiltonian [26,109,121]

$$H_{(1,1)} = \frac{b_1}{2}\sigma_z^{(1)} + \frac{b_2}{2}\sigma_z^{(2)} + \frac{J}{4}\boldsymbol{\sigma}^{(1)} R_{so} \boldsymbol{\sigma}^{(2)}. \tag{9}$$

The anisotropic exchange (assuming $U_{11} = U_{22} \equiv U$)

$$J \approx \frac{2T^2}{U_+} + \frac{2T^2}{U_-} - \frac{2T^2\Delta_\varphi^2}{U_+^2(U_{12}-\Sigma)} + \frac{2T^2\Delta_\varphi^2}{U_-^2(2U+3U_{12}-\Sigma)} \tag{10}$$

comprises a DSQ contribution $\propto T^2/U$ and an ASQ-mediated contribution $\propto T^2\Delta_\varphi^2/U^3$. We introduced $U_\pm = U - U_{12} \pm \epsilon$, $\Sigma = \epsilon_1 + \epsilon_2$, and discarded corrections $\propto b_i b_j$ and $\propto T^4$, see Appendixes. We expect $J/h \in [0\text{–}1]$ GHz in the range reached for DSQs. Because of the phase dependence of ϵ_2 and Δ_φ, J inherits an even φ-dependence, see Fig. 3(a), whose sign and amplitude depend on ϵ.

The system is coupled to the resonator by

$$H_{(1,1),I} \approx \sum_j \frac{\varphi_r^j X^j \mathbf{b}_2^{(j)} \cdot \boldsymbol{\sigma}^{(2)}}{2} + \frac{\varphi_r^j X^j J^{(j)}}{4} \boldsymbol{\sigma}^{(1)} R_{so} \boldsymbol{\sigma}^{(2)}, \tag{11}$$

where we identify two distinct contributions: the magnetic modulation of $\mathbf{b}_2$ and the charge modulation of T and ϵ_2, which yields a φ-dependent J, with susceptibility $J^{(j)} = \partial_\varphi^j J/j$. We focus on exchange-mediated processes and neglect the DSQ-ASQ spin hybridization $\propto b_i T^2/U^2$, similar to Eq. (5).

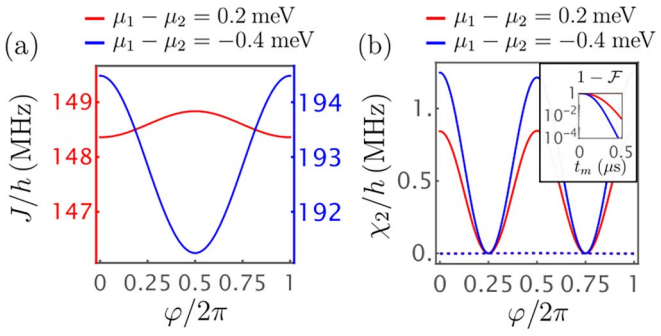

FIG. 3. ASQ-DSQ exchange interaction. (a) Phase dependence of J for positive and negative chemical potential shifts. Approaching the (2, 0) region (blue curve) or the (0, 2) region (red curve) largely increases J. (b) Dispersive (solid lines) and direct (dashed lines) resonator shifts for the same parameters as above. In the inset, we show the readout fidelity at $\varphi = 0$. We use $T/h = 2.5$ GHz and fix $\mu_2 = 1$ meV. Other parameters as in Fig. 2.

VIII. EXCHANGE-MEDIATED READOUT

The tuneable anisotropic exchange in Eq. (B23) enables different efficient readout schemes. For $b_1 \sim b_2$ and $R_{so} \sim 1$, a convenient readout protocol involves first a SWAP gate between DSQ and ASQ, implemented by activating the approximately isotropic exchange J for a time $t_{\mathrm{SWAP}} = \hbar\pi/J$ [122], followed by fast ASQ readout.

However, the anisotropic exchange interactions of Ge [109] enable exchange-mediated readout protocols. By restricting to $J \ll |b_1 - b_2|$, $H_{(1,1)}$ reduces to [123]

$$H_{(1,1)}^{\parallel} = \frac{b_1}{2}\sigma_z^{(1)} + \frac{b_2}{2}\sigma_z^{(2)} + \frac{J_\parallel}{4}\sigma_z^{(1)}\sigma_z^{(2)}, \tag{12}$$

with a tuneable Ising interaction $J_\parallel = J\mathbf{e}_z R_{so}\mathbf{e}_z$. Neglected flip-flop interactions can induce SWAP dynamics, potentially leading to readout errors. These errors are minimized by exchange anisotropies [26,79,123] and large Zeeman energy differences, which in Ge reach $(b_1 - b_2)/h(\tilde{b}_1 + b_2)/h \sim 1$ GHz at 200 mT [124]. Under these conditions, the SWAP dynamics occur on timescales approximately $h|b_1 - b_2|/J^2 \gtrsim 10$ μs at $J/h \lesssim 300$ MHz, longer than the target sub-microsecond integration time.

Because of $J_\parallel$, the ASQ Stark shift inherits a DSQ-state dependence, yielding the three-body interaction in the rotating frame $H_{(1,1),I}^R = \chi_2 \sigma_z^{(1)}\sigma_z^{(2)} a^\dagger a$, with

$$\chi_2 \approx -\frac{\varphi_r^2 J_\parallel |\mathbf{b}_2^{(1)} \times \mathbf{e}_z|^2}{16(b_2 - \hbar\omega_r)^2 - 4J_\parallel^2} + \frac{\varphi_r^2 J_\parallel^{(2)}}{4}. \tag{13}$$

With the same parameters as for the hybrid readout, halving T to suppress flip-flop terms, we estimate a dispersive coupling in the MHz range, see Fig. 3(b), exceeding the direct coupling and comparable to χ_1. The dispersive shift χ_2 enables sub-microsecond DSQ readout with reasonable fidelity by keeping the ASQ in its groundstate and detecting the DSQ-state-dependent shift of the resonator frequency. This provides an alternative route to fast and high-fidelity DSQ readout.

IX. CONCLUSION

We present tunable hybrid couplers composed of DSQs tunnel-coupled to ASQs, which are themselves inductively coupled to resonators. Focusing on germanium-based platforms, we investigate multiple readout schemes in configurations where the coupler is occupied by either one or two particles. In both regimes, we show that our architecture supports fast, high-fidelity DSQ readout within sub-microsecond timescales, enabled by dispersive, direct, or longitudinal resonator coupling. Beyond readout, our ASQ-DSQ coupler can offer a promising route to entangle distant DSQs, offering more flexible and scalable layouts for spin-based quantum processors.

ACKNOWLEDGMENTS

We acknowledge support by the EU through the H2024 QLSI2 project, the Army Research Office under Award Number: W911NF-23-1-0110, and NCCR Spin Grant No. 225153. K. L. acknowledges support by the Laboratory for Physical Sciences through the Condensed Matter Theory Center. A. C. acknowledges support from the IGNITE project under grant agreement no. 101069515 of the Horizon Europe Framework Programme, as well as the US Army Research Office under Award Number: W911NF-24-2-0043. The views and conclusions contained in this document are those of the authors and should not be interpreted as representing the official policies, either expressed or implied, of the Army Research Office or the U.S. Government. The U.S. Government is authorized to reproduce and distribute reprints for Government purposes notwithstanding any copyright notation herein.

DATA AVAILABILITY

The data that support the findings of this article are openly available at [125].

APPENDIX A: EFFECTIVE DOUBLE-DOT HAMILTONIAN

To describe the DSQ-ASQ hybrid system, we start from the Hamiltonian $H = H_{\mathrm{DQD}} + H_L + H_{L-D2}$ with

$$H_{\mathrm{DQD}} = \sum_i \mathbf{c}_i^\dagger \left(-\mu_i \sigma_0 + \frac{\mu_B g_i \mathbf{B}\cdot\boldsymbol{\sigma}}{2} \right) \mathbf{c}_i - T(\mathbf{c}_1^\dagger \tilde{S}_{so} \mathbf{c}_2 + \mathbf{c}_2^\dagger \tilde{S}_{so}^\dagger \mathbf{c}_1) + \sum_{ij,\sigma\sigma'} \frac{U_{ij}}{2} (1 - \delta_{ij}\delta_{\sigma\sigma'}) n_{i\sigma} n_{j\sigma'}, \tag{A1a}$$

$$H_L = \sum_{\alpha,k} \xi_{\alpha k} \mathbf{d}_{\alpha k}^\dagger \mathbf{d}_{\alpha k} + \left(\sum_{\alpha,k} \Delta_\alpha e^{(-1)^\alpha i\varphi/2} d_{\alpha k\uparrow}^\dagger d_{\alpha -k\downarrow}^\dagger + \sum_k t_{sc} \mathbf{d}_{1k}^\dagger S_{so}^{sc} \mathbf{d}_{2k} + \mathrm{H.c.} \right), \tag{A1b}$$

$$H_{L-D2} = \sum_{\alpha,k} t_\alpha \mathbf{d}_{\alpha k}^\dagger S_{so}^\alpha \mathbf{c}_2 + \mathrm{H.c.} \tag{A1c}$$

Equation (A1a) describes the bare double quantum dot, where $\mathbf{c}_i = (c_{i\uparrow}, c_{i\downarrow})$ is the vector of annihilation operators for electrons in dot $i \in \{1,2\}$, μ_i (g_i) is the chemical potential (g tensor) for dot i, $\mathbf{B}$ is the magnetic field, $\boldsymbol{\sigma} = (\sigma_x, \sigma_y, \sigma_z)$ is the vector of Pauli matrices acting in spin space, T is the interdot tunneling amplitude, $\tilde{S}_{so} = e^{i\tilde{\theta}_{so}\tilde{\mathbf{n}}_{so}\cdot\boldsymbol{\sigma}/2}$ describes a unitary evolution in spin space due to SOI, $n_{i\sigma} = c_{i\sigma}^\dagger c_{i\sigma}$ is the number operator, and U_{ii} ($U_{12} = U_{21}$) are Hubbard intradot (interdot) interactions. Note that here we directly subtract the diagonal term $\propto (n_{i\sigma})^2 = n_{i\sigma}$ from the Hubbard interaction, whereas this contribution is included in the single-particle energy in the main text for convenience.

Equation (A1b) describes the two superconducting leads, where $\mathbf{d}_{\alpha k} = (d_{\alpha k\uparrow}, d_{\alpha k\downarrow})$ is the vector of annihilation operators for electrons of momentum k in lead $\alpha \in \{1,2\}$, $\xi_{\alpha k}$ is the onsite energy in lead α, t_{sc} is a direct tunneling between the two leads originating from tracing out nonresonant ASQ levels, where we again account for a unitary evolution in spin space $S_{so}^{sc} = e^{i\theta_{so}^{sc}\mathbf{m}_{so}^{sc}\cdot\boldsymbol{\sigma}/2}$ due to SOI, and Δ_α is the effective pairing amplitude in lead α. Furthermore, φ is the phase difference across the junction. In the main text, we also add a resonator with energy $\hbar\omega_r a^\dagger a$ coupled inductively to the ASQ, which modifies the phase difference as $\varphi \to \varphi + \varphi_r(a + a^\dagger)/\sqrt{2}$, where $a^\dagger$, a are creation, annihilation operators for the resonator mode, respectively.

Equation (A1c) describes the coupling between the superconducting leads and the second quantum dot, which together form the ASQ. Here, t_α is the tunneling amplitude between the dot and lead α, where $S_{so}^\alpha = e^{i\theta_{so}^\alpha \mathbf{m}_{so}^\alpha\cdot\boldsymbol{\sigma}/2}$ is once again a unitary evolution in spin space due to SOI.

For simplicity, we assume the leads to be symmetric and set $\xi_{1k} = \xi_{2k} \equiv \xi_k$ with $\xi_k = \hbar^2 k^2/2m - \mu_{sc}$, $\Delta_1 = \Delta_2 \equiv \Delta_0$, and $t_1 = t_2 \equiv t$. We further consider $\theta_{so}^1 = -\theta_{so}^2 = \theta_{so}^{sc}/2$ consistent with the setup shown in Fig. 1 of the main text. For simplicity, we set $\mathbf{m}_{so}^1 = \mathbf{m}_{so}^2 = \mathbf{m}_{so}^{sc} \equiv \mathbf{m}_{so}$ here, but our results can be generalized to arbitrary rotations. In analogy to the main text, we denote with $\tilde{\mathbf{n}}_{so}$ the direction of the SOI between the DSQ and the ASQ, and with $\mathbf{m}_{so}$ the direction SOI between the superconducting leads and the ASQ, which is not generally aligned to $\tilde{\mathbf{n}}_{so}$. Moreover, in the main text we distinguish between the vector of SOIs $\tilde{\mathbf{n}}_{so}$ and the vector $\mathbf{n}_{so}$, which includes the tilts of quantization axes of between ASQ and DSQ, i.e., $U_1^\dagger e^{i\tilde{\theta}_{so}\tilde{\mathbf{n}}_{so}\cdot\boldsymbol{\sigma}/2} U_2 \equiv e^{i\theta_{so}\mathbf{n}_{so}\cdot\boldsymbol{\sigma}/2}$, where the unitary operators $U_i = e^{-i\Theta_i \mathbf{n}_i\cdot\boldsymbol{\sigma}/2}$ satisfy $U_i^\dagger(\mathbf{b}_i\cdot\boldsymbol{\sigma})U_i = b_i\sigma_z$ and align both Zeeman fields $\mathbf{b}_{i=1,2}$ to the z-direction.

We start by focusing on the large-gap limit $\Delta_0 \gg U_{ij}$. This allows us to integrate out the superconducting leads

and to derive a simple effective Hamiltonian for the ASQ-DSQ hybrid double dot. For this, we first diagonalize the leads via a standard Bogoliubov transformation $d^\dagger_{ak\uparrow} = e^{(-1)^\alpha i\varphi/4}(\cos\varphi_k\,\tilde{d}^\dagger_{ak\uparrow} + \sin\varphi_k\,\tilde{d}_{ak\downarrow})$, $d^\dagger_{\alpha-k\downarrow} = e^{(-1)^\alpha i\varphi/4}(\cos\varphi_k\,\tilde{d}^\dagger_{ak\downarrow} - \sin\varphi_k\,\tilde{d}_{ak\uparrow})$ with $\tan 2\varphi_k = \Delta_0/\xi_k$ and energy $E_k = \sqrt{\xi_k^2 + \Delta_0^2}$. Then, we perform a Schrieffer-Wolff transformation to third order in the tunnel couplings and Zeeman field to obtain an effective low-energy Hamiltonian describing the DSQ-ASQ hybrid, where the leads have now effectively been removed from the problem. This results in the effective double-dot Hamiltonian $H = H_0 + H_T$, where

$$H_0 = \sum_i \mathbf{c}_i^\dagger(-\epsilon_i\sigma_0 + \mathbf{b}_i\cdot\boldsymbol{\sigma}/2)\mathbf{c}_i - \Delta_\varphi(c^\dagger_{2\uparrow}c^\dagger_{2\downarrow} + c_{2\downarrow}c_{2\uparrow}) + \sum_{ij,\sigma\sigma'}\frac{U_{ij}}{2}(1-\delta_{ij}\delta_{\sigma\sigma'})n_{i\sigma}n_{j\sigma'}, \tag{A2a}$$

$$H_T = -T\left(\mathbf{c}_1^\dagger\tilde{S}_{so}\mathbf{c}_2 + \mathbf{c}_2^\dagger\tilde{S}^\dagger_{so}\mathbf{c}_1\right). \tag{A2b}$$

These are Eqs. (1) and (2) in the main text. Here, the effective parameters describing the DSQ in dot 1 remain unchanged compared to Eq. (A1a), i.e., we have $\epsilon_1 = \mu_1$ and $\mathbf{b}_1 = \mu_B\mathbf{B}g_1$, while the parameters describing the ASQ in dot 2 are modified by the coupling to the superconducting leads as

$$\epsilon_2 = \mu_2 + E_0\cos(\varphi), \tag{A3}$$

$$\mathbf{b}_2 = \mu_B\mathbf{B}g_2 - E_{so}\sin(\varphi)\mathbf{m}_{so}, \tag{A4}$$

$$\Delta_\varphi = \Delta\cos(\varphi/2), \tag{A5}$$

where

$$E_0 = 2t^2t_{sc}\cos(\theta^{sc}_{so})\int dk\frac{\sin^2(\varphi_k)}{E_k^2} \approx \Gamma\frac{t_{sc}}{\Delta_0}\cos(\theta^{sc}_{so}), \tag{A6}$$

$$E_{so} = 4t^2t_{sc}\sin(\theta^{sc}_{so})\int dk\frac{\sin^2(\varphi_k)}{E_k^2} \approx 2\Gamma\frac{t_{sc}}{\Delta_0}\sin(\theta^{sc}_{so}), \tag{A7}$$

$$\Delta = 2t^2\int dk\frac{\sin(\varphi_k)}{E_k} \approx 2\Gamma. \tag{A8}$$

In the approximation, we have assumed a constant density of states ρ for the leads and introduced the tunneling rate $\Gamma = \pi\rho t^2$. We neglect small corrections arising from third-order perturbation theory,

$$2t^2\int\frac{dk}{E_k^2} \approx \frac{2\Gamma}{\Delta_0}, \tag{A9}$$

which renormalize $\epsilon_2 \to \epsilon_2(1-2\Gamma/\Delta_0)$, $\mathbf{b}_2 \to \mathbf{b}_2(1-2\Gamma/\Delta_0)$, and $T \to T(1-\Gamma/\Delta_0)$ due to hybridization with the leads. These corrections are consistent with the generalized atomic-limit substitutions $1/(1+2\Gamma/\Delta_0)$ in the weak tunneling limit [92]. Similarly, we also neglect the corresponding renormalization of the Hubbard energy U_{22}.

While working in the large-gap limit has allowed us to derive a simple effective Hamiltonian for the DSQ-ASQ hybrid, current experimental systems are often in the opposite limit $U_{ij} \gg \Delta_0$. In a recent work [49], numerical renormalization group (NRG) calculations were used to confirm that the phase dependence of the ASQ parameters given in Eqs. (A6) and (A7), as well as the linear dependence of E_{so} on small Γ, t_{sc}, and θ^{sc}_{so}, remains valid up to $U \gtrsim 10\Delta_0$. Therefore, the simple effective Hamiltonian given in Eq. (A2a) can offer qualitative insights even beyond the large-gap limit. However, a more sophisticated numerical analysis is required to find the precise dependence of the ASQ parameters on Δ_0, especially in the regime $\Gamma \gtrsim \Delta_0$ [49].

In Appendix F, we additionally study a simplified version of H for $U_{ij} \gg \Delta_0$ using exact numerical diagonalization, showing that the charge stability diagram presented in Fig. 1 of the main text—which defines the operating points of the DSQ-ASQ coupler—remains qualitatively correct in the small-gap regime as long as the dot-lead tunneling is sufficiently small.

APPENDIX B: SPIN-PHOTON COUPLING

In this section, we present the full derivations underlying the equations for the spin-photon coupling used in the main text.

1. ASQ-resonator coupling

Inductive coupling of the resonator to the ASQ shifts the phase $\varphi \to \varphi + X\varphi_r$, where $X = (a^\dagger + a)/\sqrt{2}$ and φ_r is a small quantity characterizing the zero-point fluctuations of the resonator. Including the phase shift in the flux-dependent quantities in Eqs. (1) and (2) of the main text, and using a Taylor expansion up to second order in φ_r, one finds

$$\epsilon_2 = \mu_2 + E_0\cos(\varphi) \to \epsilon_2 + \varphi_r X\,\partial_\varphi\epsilon_2 + \varphi_r^2 X^2\frac{\partial_\varphi^2\epsilon_2}{2} = \epsilon_2 - E_0\,\varphi_r\,X\sin(\varphi) - \frac{E_0}{2}\,\varphi_r^2 X^2\cos(\varphi),$$
$$\mathbf{b}_2 = \mu_B\mathbf{B}g_2 - E_{so}\sin(\varphi)\mathbf{m}_{so} \to \mathbf{b}_2 + \varphi_r X\,\partial_\varphi\mathbf{b}_2 + \varphi_r^2\,X^2\frac{\partial_\varphi^2\mathbf{b}_2}{2} = \mathbf{b}_2 - \left(\varphi_r X\,E_{so}\cos(\varphi) - \frac{E_{so}}{2}\varphi_r^2\,X^2\sin(\varphi)\right)\mathbf{m}_{so},$$
$$\Delta_\varphi = \Delta\cos\left(\frac{\varphi}{2}\right) \to \Delta_\varphi + \varphi_r\,X\partial_\varphi\Delta_\varphi + \varphi_r^2\,X^2\partial_\varphi^2\Delta_\varphi = \Delta_\varphi - \frac{\Delta}{2}\varphi_r\,X\sin\left(\frac{\varphi}{2}\right) - \frac{\Delta}{8}\varphi_r^2\,X^2\cos\left(\frac{\varphi}{2}\right). \tag{B1}$$

This leads to the ASQ-resonator coupling Hamiltonian

$$H_I = \sum_{j>0}\varphi_r^j X^j\left(\mathbf{c}_2^\dagger\frac{\mathbf{b}_2^{(j)}\cdot\boldsymbol{\sigma} - 2\epsilon_2^{(j)}}{2}\mathbf{c}_2 - \Delta^{(j)}c_{2\uparrow}^\dagger c_{2\downarrow}^\dagger + \text{H.c.}\right) \tag{B2}$$

given in Eq. (3) in the main text. This coupling includes resonator-induced fluctuations of ASQ dot and Zeeman energy, $\epsilon_2^{(j)} = \partial_\varphi^j\epsilon_2/j \propto E_0$ and $\mathbf{b}_2^{(j)} = \partial_\varphi^j\mathbf{b}_2/j \propto E_{so}\mathbf{m}_{so}$, respectively, and the resonator-mediated pairing $\Delta^{(j)} = \partial_\varphi^j\Delta_\varphi/j \propto \Delta$.

2. Single-particle regime

a. Effective single-particle Hamiltonian

To derive the DQD-resonator coupling in the single-particle regime, we start from Eq. (4) in the main text:

$$H_{1\text{P}} = -\tau_z\frac{\epsilon_\varphi}{2} + \tau_1\frac{b_1\sigma_z}{2} + \tau_2\frac{b_2\sigma_z}{2} - T_\varphi(\tau_+ S_{so} + \tau_- S_{so}^\dagger), \tag{B3}$$

where the Pauli matrices τ act on the dot subspace, $\tau_\pm = (\tau_x \pm i\tau_y)/2$, and $\tau_{1,2} = (\tau_0 \pm \tau_z)/2$. We have aligned both Zeeman fields along the z-direction by a local spin rotation R_i generated by $\tau_i U_i = \tau_i e^{-i\Theta_i\mathbf{n}_i\cdot\boldsymbol{\sigma}/2}$ satisfying $U_i^\dagger(\mathbf{b}_i\cdot\boldsymbol{\sigma})U_i = (R_i\mathbf{b}_i)\cdot\boldsymbol{\sigma} = b_i\sigma_z$. In this frame, the spin-flip tunneling operator transforms as $S_{so} = U_1^\dagger\tilde{S}_{so}U_2 \equiv e^{i\theta_{so}\mathbf{n}_{so}\cdot\boldsymbol{\sigma}/2}$, with modified θ_{so} and $\mathbf{n}_{so}$. Note that by aligning the Zeeman fields along the z direction, we introduce the rotations U_1 and U_2. The rotation U_2 that aligns $\mathbf{b}_2$ along z is generally φ-dependent because $\mathbf{B}g_2$ and $\mathbf{m}_{so}$ are not necessarily aligned. From this, it follows that $S_{so} = U_1\tilde{S}_{so}U_2$ is also generally φ dependent. We neglect this dependence in this work.

We consider the case where the spin remains confined in the DSQ and hybridizes to the ASQ by $T_\varphi \lesssim \epsilon_\varphi$, assuming the particle is mostly localized in the first dot. For convenience, we first apply the unitary rotation $U = \tau_1\sigma_0 + \tau_2 S_{so}$ that moves the spin rotation from the tunneling term to the mostly unoccupied dot, resulting in

$$\begin{aligned} H'_{1\text{P}} &= -\frac{\epsilon_\varphi}{2}\tau_z + \frac{b_1}{2}\tau_1\sigma_z + \frac{b_2}{2}\tau_2 S_{so}\sigma_z S_{so}^\dagger - T_\varphi\tau_x \\ &= -\frac{\epsilon_\varphi}{2}\tau_z + \frac{b_1}{2}\tau_1\sigma_z + \frac{b_2}{2}\tau_2(R_{so}\mathbf{e}_z)\cdot\boldsymbol{\sigma} - T_\varphi\tau_x. \end{aligned} \tag{B4}$$

We then apply a standard Schrieffer-Wolff (SW) transformation up to second order in T_φ, projecting onto the subspace of the first dot. This leads to

$$H_{\text{eff}} = -\frac{\epsilon_\varphi}{2}\sigma_0 + \frac{b_1}{2}\sigma_z - T_\varphi^2\frac{\epsilon_\varphi\,\sigma_0 - \mathbf{r}\cdot\boldsymbol{\sigma}}{\epsilon_\varphi^2 - |\mathbf{r}|^2} \tag{B5}$$

with $\mathbf{r} = \frac{1}{2}(b_2(R_{so}\mathbf{e}_z) - b_1\mathbf{e}_z)$. Next, we focus on the limit $b_1, b_2 \ll \epsilon$ and expand the term $\propto T^2$ to second order, which results in

$$\begin{aligned} H_{\text{eff}} &= -\frac{\epsilon_\varphi}{2}\sigma_0 + \frac{b_1}{2}\sigma_z - \frac{T_\varphi^2}{\epsilon_\varphi^2}(\epsilon_\varphi\,\sigma_0 - \mathbf{r}\cdot\boldsymbol{\sigma}) \\ &= -\left(\frac{\epsilon_\varphi}{2} - \frac{T_\varphi^2}{\epsilon_\varphi}\right)\sigma_0 + \frac{b_1}{2}\left(1 - \frac{T_\varphi^2}{\epsilon_\varphi^2}\right)\sigma_z \\ &\quad + \frac{T_\varphi^2}{\epsilon_\varphi^2}\frac{b_2}{2}(R_{so}\mathbf{e}_z)\cdot\boldsymbol{\sigma}, \end{aligned} \tag{B6}$$

where we have discarded all terms $O(\frac{1}{\epsilon^3})$. As we are only interested in the spin physics, we also drop the constant contribution $\propto\sigma_0$ and write

$$H_{hy} = \frac{b_1}{2}(1-\eta)\sigma_z + \eta\frac{b_2}{2}(R_{so}\mathbf{e}_z)\cdot\boldsymbol{\sigma} \tag{B7}$$

with $\eta = T_\varphi^2/\epsilon_\varphi^2$. This is Eq. (5) in the main text. The flux-dependent quantities are then b_2 and η.

Alternatively, one can also directly diagonalize the orbital part of the Hamiltonian in Eq. (B4) by the transformation $U_\tau = e^{-i\tau_y\theta_\tau/2}$, with $\theta_\tau = \arctan2(2T_\varphi, \epsilon_\varphi)$. Projecting onto the lowest-energy states with orbital

energy $-\sqrt{\epsilon_\varphi^2+4T_\varphi^2}$, we find the same hybridized Hamiltonian

$$H_{hy}=\frac{b_1(1-\eta)}{2}\sigma_z+\eta\frac{b_2}{2}(R_{so}\mathbf{e}_z)\cdot\boldsymbol{\sigma}, \tag{B8}$$

with the hybridization constant

$$\eta=\frac{1}{2}-\frac{\epsilon_\varphi}{2\sqrt{\epsilon_\varphi^2+4T_\varphi^2}}=\frac{T_\varphi^2}{\epsilon_\varphi^2}+\mathcal{O}\left(\frac{T_\varphi^3}{\epsilon_\varphi^3}\right). \tag{B9}$$

As expected, the results obtained with these two approaches agree when the first dot is lower in energy ($\epsilon_\varphi>0$) and weakly hybridized to the second dot.

b. DSQ-resonator coupling

The coupling to the resonator is again obtained by shifting $\varphi\to\varphi+X\varphi_r$ in the Hamiltonian H_{hy} in Eq. (B7). A Taylor expansion up to second order in φ_r leads to the coupling Hamiltonian $H_{hy,I}=H_{hy}^{(1)}+H_{hy}^{(2)}$ with

$$\begin{aligned}H_{hy}^{(1)}&=\frac{1}{2}\left[-b_1\eta^{(1)}\sigma_z+\eta^{(1)}b_2(R_{so}\mathbf{e}_z)\cdot\boldsymbol{\sigma}+\eta b_2^{(1)}(R_{so}\mathbf{e}_z)\cdot\boldsymbol{\sigma}\right]X\varphi_r\\&=\varphi_rX\left[\eta\frac{R_{so}\mathbf{b}_2^{(1)}}{2}-\eta^{(1)}\frac{(b_1-b_2R_{so})}{2}\mathbf{e}_z\right]\cdot\boldsymbol{\sigma}\equiv\varphi_rX\boldsymbol{\gamma}^{(1)}\cdot\boldsymbol{\sigma},\\H_{hy}^{(2)}&=\varphi_r^2X^2\left[\eta\frac{(R_{so}\mathbf{b}_2^{(2)})}{2}-\eta^{(2)}\frac{(b_1\sigma_z-b_2R_{so})}{2}\mathbf{e}_z+\frac{\eta^{(1)}R_{so}\mathbf{b}_2^{(1)}}{2}\right]\cdot\boldsymbol{\sigma}\equiv\varphi_r^2X^2\boldsymbol{\gamma}^{(2)}\cdot\boldsymbol{\sigma},\end{aligned} \tag{B10}$$

with the magnetic susceptibility of the ASQ $\mathbf{b}_2^{(j)}=\partial_\varphi^j\mathbf{b}_2/j$ and the orbital susceptibility $\eta^{(j)}=\partial_\varphi^j\eta/j$. This results in the DSQ-resonator coupling

$$H_{hy,I}=(\varphi_rX\boldsymbol{\gamma}^{(1)}+\varphi_r^2X^2\boldsymbol{\gamma}^{(2)})\cdot\boldsymbol{\sigma} \tag{B11}$$

given in Eq. (6) of the main text.

c. Dispersive and direct shift

The hybridized DSQ-resonator system can be described by the Hamiltonian $H_{\mathrm{tot}}=H_{hy}+H_r+H_{hy,I}$, where the uncoupled qubit and resonator are described by

$$H_{hy}+H_r=\frac{b_{hy}}{2}\sigma_z+\hbar\omega_ra^\dagger a. \tag{B12}$$

Here, we have diagonalized the spin component of the hybridized DQD and introduced the amplitude of the DSQ splitting $b_{hy}=|[(1-\eta)b_1+\eta b_2R_{so}]\cdot\mathbf{e}_z|$. The qubit-resonator coupling $H_{hy,I}$ given in Eq. (B11) can be divided into a transversal and a longitudinal component with respect to the hybrid DQD Zeeman field

$$\begin{aligned}H_{hy,\perp}&=\varphi_rX(\gamma_x^{(1)}\sigma_x+\gamma_y^{(1)}\sigma_y)+\varphi_r^2X^2(\gamma_x^{(2)}\sigma_x+\gamma_y^{(2)}\sigma_y)\cdot\boldsymbol{\sigma},\\H_{hy,\parallel}&=\varphi_rX\gamma_z^{(1)}\sigma_z+\varphi_r^2X^2\gamma_z^{(2)}\sigma_z.\end{aligned} \tag{B13}$$

We first focus on the transversal coupling and write $\sigma_x=\sigma_++\sigma_-$ and $\sigma_y=-i(\sigma_+-\sigma_-)$, such that

$$\begin{aligned}H_{hy,\perp}&=\varphi_rX\left(\left(\gamma_x^{(1)}-i\gamma_y^{(1)}\right)\sigma_++\left(\gamma_x^{(1)}+i\gamma_y^{(1)}\right)\sigma_-\right)+\varphi_r^2X^2\left(\left(\gamma_x^{(2)}-i\gamma_y^{(2)}\right)\sigma_++\left(\gamma_x^{(2)}+i\gamma_y^{(2)}\right)\sigma_-\right)\\&=\frac{\varphi_r}{\sqrt{2}}(a^\dagger+a)\left(\alpha^{(1)}\sigma_++\alpha^{(1)*}\sigma_-\right)+\frac{\varphi_r^2}{2}(a^\dagger+a)^2\left(\alpha^{(2)}\sigma_++\alpha^{(2)*}\sigma_-\right)\end{aligned} \tag{B14}$$

with $\alpha^{(i)}=\gamma_x^{(i)}+i\gamma_y^{(i)}$. Assuming $|b_{hy}-\hbar\omega_r|\ll b_{hy}+\hbar\omega_r$ and applying a rotating wave approximation, where we drop all fast oscillating terms, leads to

$$\begin{aligned}H_{hy,\perp}&\approx\frac{\varphi_r}{\sqrt{2}}\left(\alpha^{(1)}a\sigma_++\alpha^{(1)*}a^\dagger\sigma_-\right)+\frac{\varphi_r^2}{2}(2a^\dagger a+1)\left(\alpha^{(2)}\sigma_++\alpha^{(2)*}\sigma_-\right)\\&=(g_1a\sigma_++g_1^*a^\dagger\sigma_-)+(2a^\dagger a+1)(g_2\sigma_++g_2^*\sigma_-)=V_1+V_2\end{aligned} \tag{B15}$$

with $g_i=(\frac{\varphi_r}{\sqrt{2}})^i\alpha^{(i)}$.

The SW transformation up to second order is $H_{\text{eff}} \approx H + [S, H] + \frac{1}{2}[S, [S, H]]$, where

$$S = S_1 + S_2 = \left(\frac{g_1}{\Delta} a\sigma_+ - \frac{g_1^*}{\Delta} a^\dagger \sigma_-\right) + (2a^\dagger a + 1)\left(\frac{g_2}{b_{hy}}\sigma_+ - \frac{g_2^*}{b_{hy}}\sigma_-\right), \tag{B16}$$

such that $[S_1, H_0] = -V_1$ and $[S_2, H_0] = -V_2$. We define $\Delta = b_{hy} - \hbar\omega_r$ and find

$$H_{\text{eff}} \approx H_{hy} + H_r + \frac{1}{2}[S_1, V_1] = H_{hy} + H_r + \frac{|g_1|^2}{\Delta}\left(a^\dagger a + \frac{1}{2}\right)\sigma_z + \frac{|g_1|^2}{2\Delta} \approx H_{hy} + H_r + \chi_{1,\perp} a^\dagger a \sigma_z, \tag{B17}$$

where we have expanded the commutators only keeping terms up to second order in φ_r. Note that V_2 only contributes to higher orders in φ_r and thus transversal higher-order contributions are discarded. The dispersive shift is explicitly given by

$$\chi_{1,\perp} = \frac{\varphi_r^2\left(\gamma_x^{(1)2} + \gamma_y^{(1)2}\right)}{2(b_{hy} - \hbar\omega_r)} = \frac{\varphi_r^2 |\boldsymbol{\gamma}^{(1)} \times \mathrm{e}_z|^2}{2(b_{hy} - \hbar\omega_r)}. \tag{B18}$$

Next, we consider the longitudinal coupling, which is described by the interaction Hamiltonian

$$H_{hy,\parallel} = \frac{\varphi_r}{\sqrt{2}}(a^\dagger + a)\gamma_z^{(1)}\sigma_z + \frac{\varphi_r^2}{2}(a^\dagger + a)^2\gamma_z^{(2)}\sigma_z = G_1(a^\dagger + a)\sigma_z + G_2(a^\dagger + a)^2\sigma_z \tag{B19}$$

with $G_i = (\varphi_r/\sqrt{2})^i \gamma_z^{(i)}$. Note that the terms $\propto G_1$ do not alter the energy spectrum, but could be used for longitudinal readout schemes if modulated in resonance to the resonator.

To remove the G_1 terms and show that the energy spectrum is not modified by this, we apply the transformation $U = \exp(\lambda\sigma_z(a^\dagger - a))$, where $\lambda = G_1/\hbar\omega_r$. This transforms the operators as $U^\dagger a U^\dagger = a - \lambda\sigma_z$, $U^\dagger a^\dagger U = a^\dagger - \lambda\sigma_z$, and $U^\dagger\sigma_z U = \sigma_z$. As such, the total Hamiltonian transforms as

$$\begin{aligned} U^\dagger H_{\text{tot}} U &= H_{hy} + H_r + \hbar\omega_r(-\lambda(a^\dagger + a)\sigma_z + \lambda^2\sigma_0) + G_1(a^\dagger + a)\sigma_z - 2g_1\lambda\sigma_0 \\ &\quad + G_2(a^\dagger + a)^2\sigma_z - 4G_2\lambda(a^\dagger\sigma_0 + a\sigma_0 - \lambda\sigma_z) \\ &\approx H_{hy} + H_r - \lambda\hbar\omega_r(a^\dagger + a)\sigma_z + G_1(a^\dagger + a)\sigma_z + G_2(a^\dagger + a)^2\sigma_z \\ &= H_{hy} + H_r + G_2(a^\dagger + a)^2\sigma_z, \end{aligned} \tag{B20}$$

where we have discarded higher-order terms $O(\varphi_r^3)$ as well as constant energy shifts. We then apply a rotating wave approximation and drop all fast oscillating terms under the assumption $|b_{hy} - \hbar\omega_r| \ll b_{hy} + \hbar\omega_r$, yielding

$$\begin{aligned} H &\approx H_{hy} + H_r + 2G_2\left(a^\dagger a + \frac{1}{2}\right)\sigma_z \\ &\approx H_{hy} + H_r + \chi_{1,\parallel} a^\dagger a \sigma_z. \end{aligned} \tag{B21}$$

In the second line, we have dropped the Lamb shift $\propto G_2\sigma_z$, which simply induces a shift in the qubit frequency on the order of φ_r^2 and only kept the direct resonator-qubit coupling $\chi_{1,\parallel}$.

We now define the total resonator shift $\chi_1 = \chi_{1,\perp} + \chi_{1,\parallel}$, combining direct and dispersive coupling, resulting in

$$\begin{aligned} &H_{hy,I}^R = \chi_1 a^\dagger a \sigma_z, \quad \text{with} \\ &\chi_1 \approx \frac{\varphi_r^2 |\boldsymbol{\gamma}^{(1)} \times \mathrm{e}_z|^2}{2(b_{hy} - \omega_r)} + \varphi_r^2 \boldsymbol{\gamma}^{(2)} \cdot \mathbf{e}_z. \end{aligned} \tag{B22}$$

This is Eq. (7) in the main text.

3. Two-particle regime

a. Effective two-particle Hamiltonian

Applying a Schrieffer-Wolff transformation to Eqs. (1) and (2) in the main text and retaining terms up to fourth order yields the effective exchange-coupled spin Hamiltonian

$$H_{(1,1)} = \frac{b_1}{2}\sigma_z^{(1)} + \frac{b_2}{2}\sigma_z^{(2)} + \frac{J}{4}\boldsymbol{\sigma}^{(1)} R_{so} \boldsymbol{\sigma}^{(2)}, \tag{B23}$$

with the anisotropic exchange interaction (assuming $U_{11} = U_{22} \equiv U$), as well as neglecting terms proportional to $b_i b_j$. The exchange J is given as

$$J \approx \frac{2T^2}{U_+} + \frac{2T^2}{U_-} - \frac{2T^2\Delta_\varphi^2}{U_+^2(U_{12}-\Sigma)} + \frac{2T^2\Delta_\varphi^2}{U_-^2(2U+3U_{12}-\Sigma)} + \frac{T^4(U-U_{12})(4(U-U_{12})^2+\epsilon^2)}{8((U-U_{12})^2-\frac{\epsilon^2}{4})^3}. \tag{B24}$$

The fourth-order tunneling term $\propto T^4$ only leads to a quantitative correction to the constant contribution to the exchange couplings shown in Fig. 3 of the main text, and therefore, we discarded it. Because of the φ-dependence of Δ_φ and ϵ_2, the exchange interaction J inherits an even flux-dependence of the form $J \approx J_0 + \sum_n J_n \cos(n\varphi)$.

b. DSQ-resonator coupling

The spin-photon interaction Hamiltonian is once again obtained by shifting $\varphi \to \varphi + X\varphi_r$, where the two flux-dependent quantities we have to consider are now given by b_2 and J. Performing a Taylor expansion up to second order in φ_r, the resonator coupling can be written as $H_{(1,1),I} \approx H^{(1)}_{(1,1)} + H^{(2)}_{(1,1)}$ with

$$\begin{aligned} H^{(1)}_{(1,1)} &= \varphi_r X\left[\frac{b_2^{(1)}}{2}\mathbf{e}_z\cdot\boldsymbol{\sigma}^{(2)} + \frac{J^{(1)}}{4}\boldsymbol{\sigma}^{(1)}R_{so}\boldsymbol{\sigma}^{(2)}\right] \\ &= \varphi_r X\left[\frac{\mathbf{b}_2^{(1)}}{2}\cdot\boldsymbol{\sigma}^{(2)} + \frac{J^{(1)}}{4}\boldsymbol{\sigma}^{(1)}R_{so}\boldsymbol{\sigma}^{(2)}\right], \\ H^{(2)}_{(1,1)} &= \varphi_r^2 X^2\left[\frac{\mathbf{b}_2^{(2)}}{2}\cdot\boldsymbol{\sigma}^{(2)} + \frac{J^{(2)}}{4}\boldsymbol{\sigma}^{(1)}R_{so}\boldsymbol{\sigma}^{(2)}\right]. \end{aligned} \tag{B25}$$

Thus, the total coupling Hamiltonian is

$$H_{(1,1),I} \approx \sum_j \frac{\varphi_r^j X^j \mathbf{b}_2^{(j)}\cdot\boldsymbol{\sigma}^{(2)}}{2} + \frac{\varphi_r^j X^j J^{(j)}}{4}\boldsymbol{\sigma}^{(1)}R_{so}\boldsymbol{\sigma}^{(2)} \tag{B26}$$

with $\mathbf{b}^{(j)} = \partial_\varphi^j \mathbf{b}_2/j$ and $J^{(j)} = \partial_\varphi^j J/j$. This is Eq. (11) in the main text.

c. Dispersive and direct shifts

By restricting to $J \ll |b_1 - b_2|$, $H_{(1,1)}$ can be simplified as

$$H^{\parallel}_{(1,1)} = \frac{b_1}{2}\sigma_z^{(1)} + \frac{b_2}{2}\sigma_z^{(2)} + \frac{J_\parallel}{4}\sigma_z^{(1)}\sigma_z^{(2)} \tag{B27}$$

with a tuneable exchange energy $J_\parallel = J\mathbf{e}_z R_{so}\mathbf{e}_z$, see Eq. (12) in the main text.

We define a Hamiltonian H composed of the qubit and resonator Hamiltonian

$$H = \frac{b_1}{2}\sigma_z^{(1)} + \frac{b_2}{2}\sigma_z^{(2)} + \frac{J_\parallel}{4}\sigma_z^{(1)}\sigma_z^{(2)} + \hbar\omega_r a^\dagger a. \tag{B28}$$

The resonator is only coupled to the second qubit, which allows us to work with the effective Hamiltonian

$$\tilde{H} = \frac{\omega_q}{2}\sigma_z^{(2)} + \hbar\omega_r a^\dagger a, \tag{B29}$$

where we have defined $\omega_q = b_2 + \frac{J_\parallel}{2}\sigma_z^{(1)}$. From Eq. (B26), the interaction Hamiltonian in the regime $J \ll |b_1 - b_2|$ is given by

$$H_{(1,1),I} \approx \frac{\varphi_r}{\sqrt{2}}(a^\dagger + a)\left(\frac{\mathbf{b}_2^{(1)}\cdot\boldsymbol{\sigma}^{(2)}}{2} + \frac{J_\parallel^{(1)}}{4}\sigma_z^{(1)}\sigma_z^{(2)}\right) + \frac{\varphi_r^2}{2}(a^\dagger + a)^2\left(\frac{\mathbf{b}_2^{(2)}\cdot\boldsymbol{\sigma}^{(2)}}{2} + \frac{J_\parallel^{(2)}}{4}\sigma_z^{(1)}\sigma_z^{(2)}\right). \tag{B30}$$

We distinguish longitudinal and transversal coupling between resonator and qubit, defining $\mathbf{b}_2^{(i)} = (\mathbf{b}_2^{(i)}\cdot\mathbf{e}_z)\mathbf{e}_z + \mathbf{e}_z\times(\mathbf{b}_2^{(i)}\times\mathbf{e}_z) = \mathbf{b}_{2,\parallel}^{(i)} + \mathbf{b}_{2,\perp}^{(i)}$, which yields

$$\begin{aligned} H_{I,\parallel} &= \varphi_r X\left(\frac{\mathbf{b}_{2,\parallel}^{(1)}\cdot\boldsymbol{\sigma}^{(2)}}{2} + \frac{J_\parallel^{(1)}}{4}\sigma_z^{(1)}\sigma_z^{(2)}\right) + \varphi_r^2 X^2\left(\frac{\mathbf{b}_{2,\parallel}^{(2)}\cdot\boldsymbol{\sigma}^{(2)}}{2} + \frac{J_\parallel^{(2)}}{4}\sigma_z^{(1)}\sigma_z^{(2)}\right), \\ H_{I,\perp} &= \varphi_r X\left(\frac{\mathbf{b}_{2,\perp}^{(1)}\cdot\boldsymbol{\sigma}^{(2)}}{2}\right) + \varphi_r^2 X^2\left(\frac{\mathbf{b}_{2,\perp}^{(2)}\cdot\boldsymbol{\sigma}^{(2)}}{2}\right). \end{aligned} \tag{B31}$$

We focus on the transversal coupling first. To simplify the notation, because the Pauli matrices in the interaction Hamiltonian always act on the ASQ in the second dot, we drop the superscript "(2)" for the Pauli matrices in the following equations. We can then write

$$\begin{aligned} H_{I,\perp} &= \varphi_r X \frac{1}{2}\left(b_{2,x}^{(1)}\sigma_x + b_{2,y}^{(1)}\sigma_y\right) + \varphi_r^2 X^2 \frac{1}{2}\left(b_{2,x}^{(2)}\sigma_x + b_{2,y}^{(2)}\sigma_y\right) \\ &= \varphi_r X \frac{1}{2}\left(\left(b_{2,x}^{(1)} - ib_{2,y}^{(1)}\right)\sigma_+ + \left(b_{2,x}^{(1)} + ib_{2,y}^{(1)}\right)\sigma_-\right) + \varphi_r^2 X^2 \frac{1}{2}\left(\left(b_{2,x}^{(2)} - ib_{2,y}^{(2)}\right)\sigma_+ + \left(b_{2,x}^{(2)} + ib_{2,y}^{(2)}\right)\sigma_-\right) \\ &= \frac{\varphi_r}{\sqrt{2}}(a^\dagger + a)\left(\beta^{(1)}\sigma_+ + \beta^{*(1)}\sigma_-\right) + \frac{\varphi_r^2}{2}(a^\dagger + a)^2\left(\beta^{(2)}\sigma_+ + \beta^{*(2)}\sigma_-\right) \end{aligned} \tag{B32}$$

with $\beta^{(i)} = \frac{1}{2}(b_{2,x}^{(i)} - ib_{2,y}^{(i)})$. Assuming $|\omega_q - \hbar\omega_r| \ll \omega_q + \hbar\omega_r$, we apply a rotating wave approximation and drop all fast rotating terms, which results in

$$\begin{aligned} H_{I,\perp} &\approx \frac{\varphi_r}{\sqrt{2}}(\beta^{*(1)} a^\dagger\sigma_- e^{i(\omega_r+\omega_q)t} + \beta^{(1)} a\sigma_+ e^{-i(\omega_r+\omega_q)t}) + \frac{\varphi_r^2}{2}(2a^\dagger a + 1)(\beta^{(2)}\sigma_+ e^{i\omega_q t} + \beta^{*(2)}\sigma_- e^{-i\omega_q t}) \\ &= (g_1 a\sigma_+ + g_1^* a^\dagger\sigma_-) + \varphi_r^2\left(a^\dagger a + \frac{1}{2}\right)\left(\frac{\mathbf{b}_{2,\perp}^{(2)}\cdot\boldsymbol{\sigma}^{(2)}}{2}\right) \\ &= V_1 + V_2. \end{aligned} \tag{B33}$$

Here, we have defined the resonator coupling strength as $g_1 = (\varphi_r/\sqrt{2})\beta^{(1)}$. We again apply a SW transformation up to second order and find that, in analogy to the single-particle case, the contributions of V_2 only lead to higher-order coupling effects. For this reason, we restrict ourselves to

$$H_{\text{eff}} \approx H + \frac{1}{2}[S_1, V_1], \tag{B34}$$

where $S_1 = \frac{1}{\Delta}(g_1 a\sigma_+ - g_1^* a^\dagger\sigma_-)$ and $\Delta = \omega_q - \hbar\omega_r$. Explicitly, the commutator is

$$\begin{aligned} \frac{1}{2}[S_1, V_1] &= \frac{|g_1|^2}{\Delta}\left(\sigma_+^{(2)}\sigma_-^{(2)} a a^\dagger - \sigma_-^{(2)}\sigma_+^{(2)} a^\dagger a\right) \\ &= \frac{|g_1|^2}{\Delta}\left(\sigma_z^{(2)} a^\dagger a + \frac{1}{2}\sigma_z^{(2)} + \frac{1}{2}\right) \\ &\approx \frac{|g_1|^2}{\Delta}\sigma_z^{(2)} a^\dagger a \\ &= \frac{\varphi_r^2 |\mathbf{b}_2^{(1)}\times\mathbf{e}_z|^2}{8((b_2 - \hbar\omega_r)^2 - \frac{J_\parallel^2}{4})}(b_2 - \hbar\omega_r)\sigma_z^{(2)} a^\dagger a - \frac{\varphi_r^2 J_\parallel |\mathbf{b}_2^{(1)}\times\mathbf{e}_z|^2}{16((b_2 - \hbar\omega_r)^2 - \frac{J_\parallel^2}{4})}\sigma_z^{(1)}\sigma_z^{(2)} a^\dagger a, \end{aligned} \tag{B35}$$

considering only the photon-number-dependent shift. Note that the first term does not couple the DSQ to the resonator, which is why we focus on the three-body interaction term $\propto \sigma_z^{(1)}\sigma_z^{(2)} a^\dagger a$ in the main text.

Next, we consider the longitudinal coupling. Starting from Eq. (B31), we find

$$\begin{aligned} H_{I,\parallel} &= \frac{\varphi_r}{\sqrt{2}}(a^\dagger + a)\left(\frac{b_{2,z}^{(1)}}{2} + \frac{J_\parallel^{(1)}}{4}\sigma_z^{(1)}\right)\sigma_z^{(2)} + \frac{\varphi_r^2}{2}(a^\dagger + a)^2\left(\frac{b_{2,z}^{(2)}}{2} + \frac{J_\parallel^{(2)}}{4}\sigma_z^{(1)}\right)\sigma_z^{(2)} \\ &= G_1\sigma_z^{(2)}(a^\dagger + a) + G_2\sigma_z^{(2)}(a^\dagger + a)^2. \end{aligned} \tag{B36}$$

To show once again that the linear longitudinal coupling does not affect the energy spectrum, we apply the displacement transformation $U = \exp(\lambda\sigma_z^{(2)}(a^\dagger - a))$ with $\lambda = G_1/\hbar\omega_r$. This transforms the operators as $U^\dagger a U^\dagger = a - \lambda\sigma_z^{(2)}$, $U^\dagger a^\dagger U = a^\dagger - \lambda\sigma_z^{(2)}$, and $U^\dagger\sigma_z^{(2)}U = \sigma_z^{(2)}$. Thus, the entire Hamiltonian transforms as

$$\begin{aligned} U^\dagger H U &= \tilde{H}_0 + \hbar\omega_r(-\lambda\sigma_z^{(2)}(a^\dagger + a) + \lambda^2\sigma_0^{(2)}) + G_1\sigma_z^{(2)}(a^\dagger + a) - 2\lambda\sigma_0^{(2)} \\ &\quad + G_2\sigma_z^{(2)}(a^\dagger + a)^2 - 4G_2\lambda(a^\dagger + a) + 4G_2\lambda^2\sigma_z^{(2)} \\ &\approx \tilde{H}_0 + \lambda(\lambda\hbar\omega_r - 2)\sigma_0^{(2)} + G_2\sigma_z^{(2)}(a^\dagger + a)^2 \\ &\approx \tilde{H}_0 + G_2\sigma_z^{(2)}(a^\dagger + a)^2, \end{aligned} \tag{B37}$$

where we only keep terms up to order $\mathcal{O}(\varphi_r^2)$ and drop constant energy shifts. Note that the terms $\lambda(\lambda\hbar\omega_r - 2)\sigma_0^{(2)}$ will modify the qubit frequency of the first qubit as $(b_1/2 + \varphi_r J_\parallel^{(1)}(\varphi_r/2\ b_{2,z}^{(1)} - 1))\sigma_z^{(1)}$. Performing a rotation wave approximation and dropping all fast oscillating terms, we end up with

$$\begin{aligned} H &= \tilde{H}_0 + G_2\sigma_z^{(2)}(2a^\dagger a + 1) \\ &= \tilde{H}_0 + \frac{\varphi_r^2}{2}\left(\frac{b_{2,z}^{(2)}}{2} + \frac{J_\parallel^{(2)}}{4}\sigma_z^{(1)}\right)\sigma_z^{(2)}(2a^\dagger a + 1) \\ &\approx \tilde{H}_0 + \frac{\varphi_r^2 J_\parallel^{(2)}}{4}\sigma_z^{(1)}\sigma_z^{(2)}a^\dagger a. \end{aligned} \tag{B38}$$

Focusing on the three-body term, we consider the coupling Hamiltonian $H_{(1,1),I}^R = \chi_2\,\sigma_z^{(1)}\sigma_z^{(2)}a^\dagger a$ with

$$\chi_2 \approx -\frac{\varphi_r^2 J_\parallel |\mathbf{b}_2^{(1)} \times \mathbf{e}_z|^2}{16(b_2 - \hbar\omega_r)^2 - 4J_\parallel^2} + \frac{\varphi_r^2 J_\parallel^{(2)}}{4}, \tag{B39}$$

which includes the dispersive and direct contributions given in Eqs. (B35) and (B38), respectively. This is Eq. (13) in the main text.

APPENDIX C: READOUT FIDELITY WITH RELAXATION

In this section, we discuss how the readout fidelity of Fig. 2(d) is impacted by a finite relaxation time T_1. For integration times much shorter than the relaxation time, $t_m \ll T_1$, the readout fidelity can be approximated as [126]

$$\mathcal{F} \approx e^{-t_m/2T_1}\mathrm{erf}\left(\frac{\mathrm{SNR(t_m)}}{2}\right) = \mathrm{e}^{-\mathrm{t_m}/\ 2\mathrm{T_1}}\mathcal{F}_0, \tag{C1}$$

where $\mathcal{F}_0$ denotes the ideal readout fidelity arising from the discrimination error of the states in the absence of relaxation processes and depends only on the signal-to-noise ratio accumulated during the measurement time t_m.

Table I summarizes the estimated readout fidelities $\mathcal{F}$ for three different readout mechanisms, evaluated for two integration times t_m and two values of the relaxation time T_1. Because there are no current ASQ devices implemented in planar Ge, we consider experimental values from ASQ experiments conducted in Al/InAs nanowires, see Ref. [48], where $T_1 \approx 11$ μs have been reported. We therefore assume that $T_1 = 10$ μs could be reached also in planar Ge. We also estimate the readout fidelity with the optimistic value $T_1 = 50$ μs.

The estimated readout fidelity approaches $\mathcal{F} \approx 0.99$ for all three readout schemes when $T_1 = 50$ μs. Shorter relaxation time $T_1 = 10$ μs causes the fidelity to reduce to approximately 95% for the slowest readout schemes, but remains above 98% for faster readouts. We therefore believe that our protocol can yield high-fidelity readout in near-future devices also when including relaxation.

APPENDIX D: ESTIMATION OF ASQ PARAMETERS IN GERMANIUM

Here, we estimate a possible range of the relevant parameters for unstrained germanium (Ge) channels confined along the z direction. The 2D Hamiltonian for an unstrained Ge hole gas and long wavelengths up to third order in momentum $k_{x,y}$ is [90]

$$H = \frac{\hbar^2(k_x^2 + k_y^2)}{2m^*} + i\sigma_+(\beta_1 k_- - \beta_2 k_+^3 + \beta_3 k_- k_+ k_-) + \mathrm{H.c.}, \tag{D1}$$

TABLE I. Table of the $\mathcal{F}_0$ associated with the corresponding integration times t_m, as well as the fidelities $\mathcal{F}$ for two different T_1 times. This is for a single particle.

Readout	t_m (μs)	$\mathcal{F}_0$	$\mathcal{F}$ at $T_1 = 10$ μs	$\mathcal{F}$ at $T_1 = 50$ μs
Dispersive	1	0.999	0.951	0.989
Direct	0.25	0.999	0.986	0.996
Longitudinal	1	0.999	0.951	0.989

where $k_\pm = k_x \pm ik_y$, $\sigma_\pm = (\sigma_x \pm \sigma_y)/2$, m^* is the effective 2D mass of the holes, and $\beta_{1,2,3}$ characterize the SOI. The unstrained nature of the channel, demonstrated in current experiments [71], enables a large enhancement of the SOI, which is required for ASQs in the absence of magnetic fields. Because $\beta_3/\beta_2 \approx (\gamma_3 - \gamma_2)/(\gamma_3 + \gamma_2) \approx 0.14$, we neglect anisotropies in the effective Hamiltonian here and set $\beta_3 = 0$. We introduce here the material-dependent Luttinger-Kohn parameters $\gamma_{1,2,3}$. This term results in an enhanced SOI for confinement along the [110]-direction. We also note that typically $\beta_1 \sim 0$ in 2D heavy hole (HH) gasses and neglect it here. Larger SOI is expected in light hole (LH) gasses [74].

Here, we focus on the buried unstrained Ge channel demonstrated experimentally in Ref. [71], which is characterized by $\beta_2 \approx 850$ meV nm^3 and $m_0/m^* \approx 13$, where m_0 is the bare electron mass. We note that current strained Ge quantum wells have a dramatically lower SOI, roughly 1–2 orders of magnitude smaller ($\beta_2 \sim 0.9$ meV nm^3 at a 1 V/μm gate field), thus leading to a much smaller spin splitting. This estimation for β_2 comes from a third-order Schrieffer-Wolff transformation starting from the six-dimensional Luttinger-Kohn Hamiltonian including HH, LH, and split-off holes (SO), see the Appendix of Ref. [71] for more details on the procedure, which leads to the Hamiltonian in Eq. (D1). The amplitude of the SOI is explicitly given by

$$\beta_2 = \left(\frac{\hbar^2}{2m_0}\right)^2 \sum_j \frac{T^{\mathrm{x}}_{1,j}\mu^*_{1,j} + \mu_{1,j}T^{\mathrm{x}*}_{1,j}}{(E^{\mathrm{H}}_1 - E^{\eta}_j)} - \frac{1}{2}\left(\frac{\hbar^2}{2m_0}\right)^3 \sum_{j,j'} \frac{T^{\mathrm{x}}_{1,j}T^{\eta}_{j,j'}T^{\mathrm{x}*}_{1,j'}}{(E^{\mathrm{H}}_1 - E^{\eta}_j)(E^{\mathrm{H}}_1 - E^{\eta}_{j'})}, \tag{D2}$$

where $E^{\mathrm{H}}_{l=1}$ and E^{η}_j are the (spin-independent) energies at $k_x = k_y = 0$ of the HH ground state and of the jth LH/SO subband, respectively (η labels subbands of pseudo-spin 1/2, which can be either LH-like or SO-like). The coefficients T and μ are given by

$$\mu_{l,j} = \frac{3}{2}\langle f^h_l|\gamma_2 + \gamma_3|f^\circ_j\rangle, \tag{D3}$$

$$T^{\mathrm{x}}_{l,j} = -\frac{3i}{\sqrt{2}}\langle f^h_l|\left(u_+|f^z_j\rangle + \frac{7\sqrt{6}}{12}[q,k_z]|f^\ell_j\rangle\right), \tag{D4}$$

$$T^{\eta}_{j,j'} = -\frac{3i}{\sqrt{2}}\left(\langle f^\circ_j|u_+|f^z_{j'}\rangle - \langle f^z_j|u_-|f^\circ_{j'}\rangle\right) - 5i\langle f^\ell_j|[q,k_z]|f^\ell_{j'}\rangle, \tag{D5}$$

$$u_\pm = \{\gamma_3, k_z\} \pm [\kappa, k_z], \tag{D6}$$

where $\langle z|f^h\rangle \equiv f^h(z)$ is the envelope function of HH subbands, and $|f^\ell_j\rangle$ is the envelope function of the LH spinor component of the jth LH/SO subband. $\{A,B\} = AB + BA$ is the anti-commutator. We also introduce the Luttinger-Kohn parameters κ and q. Finally, the envelopes $|f^\circ\rangle$ and $|f^z\rangle$ are linear combinations of $|f^\ell\rangle$ and $|f^s\rangle$:

$$|f^z_j\rangle \equiv \frac{1}{\sqrt{3}}(\sqrt{2}|f^\ell_j\rangle - |f^s_j\rangle), \tag{D7a}$$

$$|f^\circ_j\rangle \equiv \frac{1}{\sqrt{3}}(|f^\ell_j\rangle + \sqrt{2}|f^s_j\rangle), \tag{D7b}$$

where $|f^s_j\rangle$ is the SO spinor component of the jth LH/SO subband. The effective mass is calculated similarly to β_2, but its exact description in terms of the envelopes and subband energies at $k_x = k_y = 0$ only requires a second-order Schrieffer-Wolff transformation. The inverse effective mass is given by

$$\frac{m_0}{m^*} = \langle f^h_1|\gamma + \gamma_2|f^h_1\rangle - \frac{\hbar^2}{2m_0}\left(\sum_l \frac{T^{\mathrm{H}}_{1,l}T^{\mathrm{H}}_{l,1}}{E^{\mathrm{H}}_1 - E^{\mathrm{H}}_l} + \sum_j \frac{T^{\mathrm{x}}_{1,j}T^{\mathrm{x}*}_{1,j}}{E^{\mathrm{H}}_1 - E^{\eta}_j}\right) \tag{D8}$$

where

$$T^{\mathrm{H}}_{l,l'} = -\frac{3i}{2}\langle f^h_l|[q,k_z]|f^h_{l'}\rangle. \tag{D9}$$

The envelope functions $|f\rangle$ and associated energies are computed by diagonalizing the 6-band $k\cdot p$ Hamiltonian evaluated at $k_x = k_y = 0$. Using the basis ordering

$$\{\mathrm{LH}+, \mathrm{SO}+, \mathrm{HH}+, \mathrm{LH}-, \mathrm{SO}-, \mathrm{HH}-\}, \tag{D10}$$

where $\pm$ labels the positive and negative spin projection along the z direction, the $k\cdot p$ Hamiltonian is given by

$$H^{k\cdot p}_0 = \begin{bmatrix} H_{\sigma=+} & 0 \\ 0 & H_{\sigma=-} \end{bmatrix}, \tag{D11a}$$

$$H_\sigma = H^k_\sigma + H^\varepsilon_\sigma + V, \tag{D11b}$$

where

$$H^k_\sigma = \tfrac{\hbar^2}{2m_0}\begin{bmatrix} -k_z\gamma_+k_z & 2\sqrt{2}\sigma k_z\gamma_2 k_z & 0 \\ & -k_z\gamma_1 k_z & 0 \\ \dagger & & -k_z\gamma_- k_z \end{bmatrix}, \tag{D12a}$$

$$H^\varepsilon_\sigma = a_v \mathrm{Tr}\,\varepsilon + b\cdot\delta\varepsilon \begin{bmatrix} -1 & \sqrt{2}\sigma & 0 \\ & 0 & 0 \\ \dagger & & 1 \end{bmatrix}, \tag{D12b}$$

$$V = \mathcal{E}_{\Gamma_5^+} + \frac{\delta_0}{3} + eF_z z - \delta_0 \begin{bmatrix} 0 & 0 & 0 \\ & 1 & 0 \\ \dagger & & 0 \end{bmatrix}. \tag{D12c}$$

Here, $\gamma_\pm = \gamma_1 \pm 2\gamma_2$ are combinations of Luttinger parameters, a_v and b are strain deformation potentials, $\delta\varepsilon = \varepsilon_{xx} - \varepsilon_{zz} \approx 1.67\varepsilon_{xx}$, where ε_{ij} is the strain tensor, δ_0 is the bulk split-off gap, and $\mathcal{E}_{\Gamma_5^+}$ is the valence band edge energy without SOI, and F_z is an electric field applied perpendicular to the 2D plane. We consider $F_z = 0.05$ V/μm and $\varepsilon_{xx} = -0.018\%$ in the Ge layer, which is consistent with the experimental values reported in Ref. [71]. The strain in the SiGe barrier is calculated assuming pseudomorphic growth. The energy band offsets between Ge and SiGe, the deformation potential constant b, the γ_i Luttinger parameters, and the g-factor parameters κ and q are parameterized as in Ref. [71]. We stress that each material parameter (γ_1, a_v, $\mathcal{E}_{\Gamma_5^+}$, etc.) is a function of the position z in the heterostructure. Because of this spatial dependence, these parameters do not commute with k_z and we treat them as diagonal operators in Eq. (D11a). The k_z operators are implemented using a finite difference scheme with a $\delta z = 0.01$ nm mesh spacing.

We consider a range of devices with typical experimental parameters for Ge, i.e., a channel along the y direction of length $l_y \in [120\text{–}200]$nm, corresponding to the orbital energy gap $\omega_y/2\pi = \hbar/2\pi m^* l_y^2 \in [16-6]$GHz, and with lateral confinement energy $\hbar\omega_x = \hbar^2/m^* l_x^2 \in [0.4\text{–}2.5]$ meV, corresponding to a confinement length $l_x \in [50-20]$nm.

The SOI angle $\theta_{so}^{sc} \approx l_y/l_{so}^{sc}$ is given by the ratio of the long confinement direction l_y and the SOI length $l_{so}^{sc} = \hbar/m^* v_{so}^{sc}$, which depends on the effective mass m^* and SOI velocity v_{so}^{sc} of the channel. To estimate this in the unstrained Ge channel, we project the cubic Rashba SOI onto the ground state in the lateral confinement x direction, with spatial extension l_x, resulting in $\hbar v_{so}^{sc} \approx 3\beta_2/2l_x^2 \in [0.5\text{–}3.2]$ meV/nm. This results in $l_{so}^{sc} \in [5.8-0.9]$ μm, and consequently in $\theta_{so}^{sc} \in [0.02\text{–}0.21]$.

We note that the SOI in this case is predominantly aligned in the lateral confinement x direction, i.e., $\mathbf{m}_{so} \approx \mathbf{e}_x$, although tilts of the order of β_3/β_2 are expected if the confinement direction is misaligned to the crystal axis. Large tilts can also originate because of inhomogeneous shear strain [87].

We emphasize that this is a conservative estimate for v_{so}^{sc} and θ_{so}^{sc} that does not account for the additional increase of linear SOI β_1 that is caused by lateral confinement [72] and inhomogeneous gate-induced strain [87]. These effects are known to drastically enlarge the resulting SOI.

To estimate the ASQ energies, we consider a Ge ASQ proximitized with platinum germanosilicide (PtSiGe) leads, where $\Delta_0 \approx 75$ μeV ($\Delta_0/h \approx 18$ GHz) [54]. We restrict the tunneling hybridization to a fraction of the gap $\Gamma \in [10\text{–}20]$ μeV ($\Gamma/h \in [2.4\text{–}4.8]$ GHz), where the results of our perturbative model are applicable. However, we expect our results to remain qualitatively valid for a broader range of tunnelings, including the limit $\Gamma \gtrsim \Delta_0$ which is reachable in current experiments in hybrid Ge systems [54], see the discussion in Appendix F and, e.g., NRG calculations [49]. Larger superconducting gaps and tunnelings are enabled by utilizing other superconductors such as aluminum or niobium. The tunneling t_{sc} through nonresonant states is required for ASQs and depends on the contributions of all excited states. We assume it to be of the same order as Γ, and setting $t_{sc} = \Gamma$, we find the range $E_{so}/h \in [10\text{–}600]$ MHz and $E_0/h \in [300\text{–}1300]$ MHz.

In the main text, we consider ASQ parameters that are well within the range discussed here. In particular, we use $E_{so}/h = 350$ MHz, $E_0/h = 900$ MHz, $\Delta/h = 8$ GHz, that are obtained for unstrained Ge wells proximitized by PtSiGe with $\Gamma/h = t_{sc}/h = 4$ GHz, $l_x = 20$ nm, and $l_y = 180$ nm.

APPENDIX E: EFFECTIVE MANY-BODY HAMILTONIAN

Starting from Eq. (A2), we can write down the full many-body Hamiltonian for the two dots (ASQ and DSQ) occupied by a maximum of 4 particles. This gives us an effective 16×16 Hamiltonian that splits into two decoupled blocks corresponding to even and odd total parity. The structure of this Hamiltonian resembles that of a conventional double quantum dot with the important difference that the $(n,0)$ and $(n,2)$ (for $n \in \{0,1,2\}$) charge sectors are coupled by the effective pairing $\propto \Delta_\varphi$ on dot 2.

We can write the effective Hamiltonian as

$$H = \begin{pmatrix} H_0 & 0 & H_{02} & 0 & 0 \\ 0 & H_1 & 0 & H_{13} & 0 \\ H_{02}^\dagger & 0 & H_2 & 0 & H_{24} \\ 0 & H_{13}^\dagger & 0 & H_3 & 0 \\ 0 & 0 & H_{24}^\dagger & 0 & H_4 \end{pmatrix}, \tag{E1}$$

where H_n in the diagonal represents the Hamiltonian of the nth charge sector and $H_{nn'}$ couples charge sectors n and n' by the superconducting correlations. Explicitly,

$$H_0 = 0, \tag{E2a}$$

$$H_1 = \begin{pmatrix} -\epsilon_1\sigma_0 + \mathbf{b}_1\cdot\boldsymbol{\sigma}/2 & -T\tilde{S}_{so} \\ -T\tilde{S}_{so}^{\dagger} & -\epsilon_2\sigma_0 + \mathbf{b}_2\cdot\boldsymbol{\sigma}/2 \end{pmatrix}, \tag{E2b}$$

$$H_2 = \begin{pmatrix} U_{11} - 2\epsilon_1 & 0 & \Theta \\ 0 & U_{22} - 2\epsilon_2 & 0 \\ \Theta^{\dagger} & 0 & (U_{12} - \epsilon_1 - \epsilon_2)\sigma_0^{(1)}\sigma_0^{(2)} + \mathbf{b}_1\cdot\boldsymbol{\sigma}^{(1)}\sigma_0^{(2)}/2 + \sigma_0^{(1)}\mathbf{b}_2\cdot\boldsymbol{\sigma}^{(2)}/2 \end{pmatrix}, \tag{E2c}$$

$$\Theta = T\begin{pmatrix} -in_+\sin(\tilde{\theta}_{so}/2) & -\cos(\tilde{\theta}_{so}/2) + in_z\sin(\tilde{\theta}_{so}/2) & \cos(\tilde{\theta}_{so}/2) + in_z\sin(\tilde{\theta}_{so}/2) & in_-\sin(\tilde{\theta}_{so}/2) \\ in_+\sin(\tilde{\theta}_{so}/2) & -\cos(\tilde{\theta}_{so}/2) - in_z\sin(\tilde{\theta}_{so}/2) & \cos(\tilde{\theta}_{so}/2) - in_z\sin(\tilde{\theta}_{so}/2) & -in_-\sin(\tilde{\theta}_{so}/2) \end{pmatrix}, \tag{E2d}$$

$$H_3 = \begin{pmatrix} (U_{22} + 2U_{12} - 2\epsilon_2 - \epsilon_1)\sigma_0 + \mathbf{b}_1\cdot\boldsymbol{\sigma}/2 & T\tilde{S}_{so}^{\dagger} \\ T\tilde{S}_{so} & (U_{11} + 2U_{12} - 2\epsilon_1 - \epsilon_2)\sigma_0 + \mathbf{b}_2\cdot\boldsymbol{\sigma}/2 \end{pmatrix}, \tag{E2e}$$

$$H_4 = U_{11} + U_{22} + 4U_{12} - 2\epsilon_1 - 2\epsilon_2. \tag{E2f}$$

Here, $n_\pm = (\tilde{\mathbf{n}}_{so})_1 \pm i(\tilde{\mathbf{n}}_{so})_2$, $n_z = (\tilde{\mathbf{n}}_{so})_3$. If we include superconducting correlations in both dots $\Delta^{(1)}$ and $\Delta^{(2)}$, we find

$$H_{02} = (\Delta^{(1)}, \Delta^{(2)}, 0, 0, 0, 0), \tag{E3a}$$

$$H_{13} = \mathrm{diag}(\Delta^{(2)}, \Delta^{(2)}, \Delta^{(1)}, \Delta^{(1)}), \tag{E3b}$$

$$H_{24} = (\Delta^{(2)}, \Delta^{(1)}, 0, 0, 0, 0)^T. \tag{E3c}$$

In this work, only dot 2 is proximitized, so we set $\Delta^{(1)} = 0$ and $\Delta^{(2)} = \Delta_\varphi$.

Starting from the full Hamiltonian given here, the effective Hamiltonians for the different charge sectors given in Eqs. (4) and (9) of the main text are then readily obtained by standard Schrieffer-Wolff perturbation theory.

APPENDIX F: EXACT DIAGONALIZATION IN THE ZERO-BANDWIDTH LIMIT

To obtain a simple model for which the many-body problem can be solved exactly, we make use of the so-called zero-bandwidth approximation (ZBA) for the superconducting leads [91]. Within this approximation, the superconducting leads are replaced by just a single site each, leading to a simplified version of the Hamiltonian terms given in Eqs. (A1b) and (A1c):

$$H_L^{ZBA} = -\mu_{sc}\sum_\alpha \mathbf{d}_\alpha^\dagger\mathbf{d}_\alpha + \left(\Delta_0\sum_\alpha e^{(-1)^\alpha i\varphi/2} d_{\alpha\uparrow}^\dagger d_{\alpha\downarrow}^\dagger + t_{sc}\mathbf{d}_1^\dagger S_{so}^{sc}\mathbf{d}_2 + \mathrm{H.c.}\right), \tag{F1}$$

$$H_{L-D2}^{ZBA} = t\sum_\alpha \mathbf{d}_\alpha^\dagger S_{so}^\alpha \mathbf{c}_2 + \mathrm{H.c.}, \tag{F2}$$

where $\mathbf{d}_\alpha = (d_{\alpha\uparrow}, d_{\alpha\downarrow})$. Here, we have again assumed symmetric leads. The resulting many-body Hamiltonian takes the form of a 256×256 matrix (4 dots occupied by a maximum of 8 particles), which can be diagonalized numerically. This approach allows us to go beyond the large-gap regime $\Delta_0 \gg U_{ij}$, where our analytical calculations were performed (see Appendix A). In Fig. 4, we show examples of charge stability diagrams for the DSQ-ASQ hybrid obtained for $\Delta_0 = 0.1U$ (here, $U_{11} = U_{22} = 4U_{12} \equiv U$) at zero phase difference $\varphi = 0$ and zero magnetic field $\mathbf{B} = 0$. In the weak-coupling limit $t \ll U$, the charge stability diagram takes the form of that of a conventional double quantum dot, see Fig. 4(a). As the tunnel coupling is increased, the quasiparticles in the

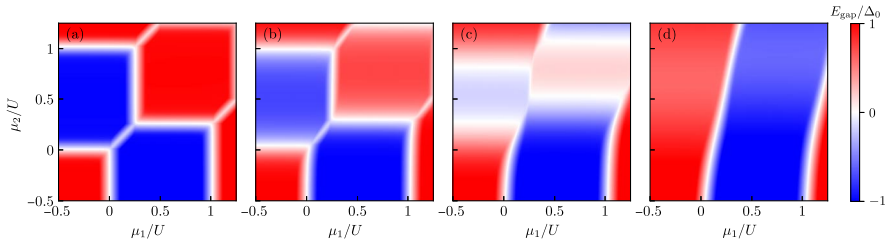

FIG. 4. Charge stability diagrams obtained from exact numerical diagonalization of $H_{DQD} + H_L + H_{L-D2}$ using the zero-bandwidth approximation for the superconducting leads. We have set $U_{11} = U_{22} = 4U_{12} \equiv U$ and (a) $t = 2t_{sc} = 0.01U$, (b) $t = 2t_{sc} = 0.05U$, (c) $t = 2t_{sc} = 0.1U$, and (d) $t = 2t_{sc} = 0.2U$. The other parameters are $\Delta_0 = 0.1U$, $\varphi = 0$, $\mu_{sc} = 0$, $T = 0.01U$, $\mathbf{B} = 0$, $\tilde{\theta}_{so} = \theta^1_{so} = -\theta^2_{so} = \theta^{sc}_{so}/2 = \pi/5$, $\tilde{\mathbf{n}}_{so} = \mathbf{m}^1_{so} = \mathbf{m}^2_{so} = \mathbf{m}^{sc}_{so} = (0, 0, 1)$. The color indicates the size of the gap between the ground state manifold and the first excited state. We have multiplied the excitation energies in the doublet sector by a factor of -1 such that different colors are assigned to sectors with singlet (red) and doublet (blue) ground states. Note that we have ignored the small splitting between singlet and triplet states in the (1, 1) sector arising due to the finite T; the excitation gap indicated for this sector corresponds to the gap between the highest-energy triplet state and the next excited state.

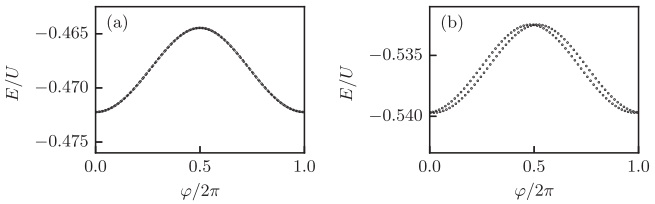

FIG. 5. Phase dependence of lowest-energy states in the (1, 0) sector obtained from exact numerical diagonalization of $H_{\rm DQD} + H_L + H_{L-D2}$ using the zero-bandwidth approximation for the superconducting leads. We have set $U_{11} = U_{22} = 4U_{12} \equiv U$ and (a) $T = 0.01U$, (b) $T = 0.15U$. The other parameters are $\mu_1 = 0.25U$, $\mu_2 = 0$, $\Delta_0 = 0.1U$, $\mu_{sc} = 0$, $t = 2t_{sc} = 0.05U$, $\mathbf{B} = 0$, $\tilde{\theta}_{so} = \theta^1_{so} = -\theta^2_{so} = \theta^{sc}_{so}/2 = \pi/5$, $\tilde{\mathbf{n}}_{so} = \mathbf{m}^1_{so} = \mathbf{m}^2_{so} = \mathbf{m}^{sc}_{so} = (0, 0, 1)$.

superconducting leads begin to screen the electron spin on dot 2 for the (0, 1) and (1, 1) sectors, see Figs. 4(b) and 4(c). Nevertheless, the doublet ground state for dot 2 still survives in some regions of parameter space. Finally, once the tunnel-coupling reaches a critical value, the spin on dot 2 is fully screened, resulting in a singlet state on dot 2 regardless of the dot energy, see Fig. 4(d).

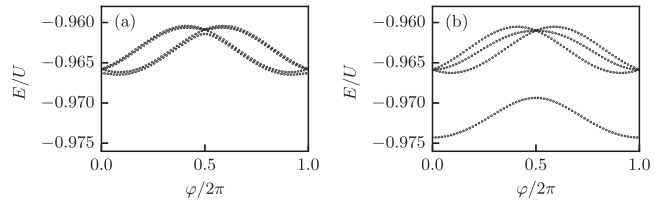

FIG. 6. Phase dependence of lowest-energy states in the (1, 1) sector obtained from exact numerical diagonalization of $H_{\rm DQD} + H_L + H_{L-D2}$ using the zero-bandwidth approximation for the superconducting leads. We have set $U_{11} = U_{22} = 4U_{12} \equiv U$ and (a) $T = 0.01U$, (b) $T = 0.04U$. The other parameters are $\mu_1 = \mu_2 = 0.5U$, $\Delta_0 = 0.1U$, $\mu_{sc} = 0$, $t = 2t_{sc} = 0.05U$, $\mathbf{B} = 0$, $\tilde{\theta}_{so} = \theta^1_{so} = -\theta^2_{so} = \theta^{sc}_{so}/2 = \pi/5$, $\tilde{\mathbf{n}}_{so} = \mathbf{m}^1_{so} = \mathbf{m}^2_{so} = \mathbf{m}^{sc}_{so} = (0, 0, 1)$.

In Fig. 5, we additionally show the phase dependence of the lowest many-body energy levels deep in the (0, 1) sector. We observe that an effective phase-dependent spin splitting is induced for the electron confined to the DSQ due to hybridization with the ASQ if the DSQ-ASQ tunneling T becomes large enough, $T \lesssim \epsilon$.

The phase dependence of the lowest-energy levels in the (1,1) sector is shown in Fig. 6. Here, we find that a phase-dependent splitting between singlet and triplet states is obtained due the effective exchange between the spin confined in the DSQ and the spin confined in the ASQ. This behavior is qualitatively consistent with the effective exchange Hamiltonian presented in the main text.

We note that while the ZBA has allowed us to work with a very simple numerically tractable model, the applicability of this model is limited due to the absence of a continuum in the superconducting leads. Nevertheless, for a single dot coupled to two superconducting leads, it has been shown that the ZBA qualitatively captures many features of the full model [93], including the singlet-doublet transition. In the case of a double-dot coupled to two leads in parallel or in series, it was found that the limitations of the ZBA become more severe [94]. However, in our case, only dot 2 is directly coupled to the SC leads, such that we expect the ZBA to give reasonable results at least as long as the interdot tunneling T is not too large. More sophisticated numerical techniques such as, e.g., NRG or a multisite extension of the ZBA could be used to verify the results presented here at a more quantitative level, which is, however, beyond the scope of this work.

[1] D. Loss and D. P. DiVincenzo, Quantum computation with quantum dots, Phys. Rev. A **57**, 120 (1998).

[2] G. Scappucci, C. Kloeffel, F. A. Zwanenburg, D. Loss, M. Myronov, J.-J. Zhang, S. De Franceschi, G. Katsaros, and M. Veldhorst, The germanium quantum information route, Nat. Rev. Mater. **6**, 926 (2021).
[3] G. Burkard, T. D. Ladd, A. Pan, J. M. Nichol, and J. R. Petta, Semiconductor spin qubits, Rev. Mod. Phys. **95**, 025003 (2023).
[4] P. Stano and D. Loss, Review of performance metrics of spin qubits in gated semiconducting nanostructures, Nat. Rev. Phys. **4**, 672 (2022).
[5] S. Neyens *et al.*, Probing single electrons across 300-mm spin qubit wafers, Nature (London) **629**, 80 (2024).
[6] R. Maurand, X. Jehl, D. Kotekar-Patil, A. Corna, H. Bohuslavskyi, R. Laviéville, L. Hutin, S. Barraud, M. Vinet, M. Sanquer, and S. De Franceschi, A CMOS silicon spin qubit, Nat. Commun. **7**, 1 (2016).
[7] N. Piot, B. Brun, V. Schmitt, S. Zihlmann, V. P. Michal, A. Apra, J. C. Abadillo-Uriel, X. Jehl, B. Bertrand, H. Niebojewski, L. Hutin, M. Vinet, M. Urdampilleta, T. Meunier, Y.-M. Niquet, R. Maurand, and S. D. Franceschi, A single hole spin with enhanced coherence in natural silicon, Nat. Nanotechnol. **17**, 1072 (2022).
[8] L. C. Camenzind, S. Geyer, A. Fuhrer, R. J. Warburton, D. M. Zumbühl, and A. V. Kuhlmann, A hole spin qubit in a fin field-effect transistor above 4 kelvin, Nat. Electron. **5**, 178 (2022).
[9] S. Bosco, S. Geyer, L. C. Camenzind, R. S. Eggli, A. Fuhrer, R. J. Warburton, D. M. Zumbühl, J. C. Egues, A. V. Kuhlmann, and D. Loss, Phase-driving hole spin qubits, Phys. Rev. Lett. **131**, 197001 (2023).
[10] S. Bosco, B. Hetényi, and D. Loss, Hole spin qubits in Si finfets with fully tunable spin-orbit coupling and sweet spots for charge noise, PRX Quantum **2**, 010348 (2021).
[11] L. Petit, H. G. J. Eenink, M. Russ, W. I. L. Lawrie, N. W. Hendrickx, S. G. J. Philips, J. S. Clarke, L. M. K. Vandersypen, and M. Veldhorst, Universal quantum logic in hot silicon qubits, Nature (London) **580**, 355 (2020).
[12] X. Xue *et al.*, CMOS-based cryogenic control of silicon quantum circuits, Nature (London) **593**, 205 (2021).
[13] A. M. J. Zwerver *et al.*, Qubits made by advanced semiconductor manufacturing, Nat. Electron. **5**, 184 (2022).
[14] H. C. George *et al.*, 12-spin-qubit arrays fabricated on a 300 mm semiconductor manufacturing line, Nano Lett. **25**, 793 (2025).
[15] P. Steinacker *et al.*, Industry-compatible silicon spin-qubit unit cells exceeding 99% fidelity, Nature (London) **646**, 81 (2025).
[16] D. Jirovec, A. Hofmann, A. Ballabio, P. M. Mutter, G. Tavani, M. Botifoll, A. Crippa, J. Kukucka, O. Sagi, F. Martins, J. Saez-Mollejo, I. Prieto, M. Borovkov, J. Arbiol, D. Chrastina, G. Isella, and G. Katsaros, A singlet-triplet hole spin qubit in planar Ge, Nat. Mater. **20**, 1106 (2021).
[17] J. Yoneda, K. Takeda, T. Otsuka, T. Nakajima, M. R. Delbecq, G. Allison, T. Honda, T. Kodera, S. Oda, Y. Hoshi, N. Usami, K. M. Itoh, and S. Tarucha, A quantum-dot spin qubit with coherence limited by charge noise and fidelity higher than 99.9%, Nat. Nanotechnol. **13**, 102 (2018).
[18] K. Takeda, A. Noiri, T. Nakajima, T. Kobayashi, and S. Tarucha, Quantum error correction with silicon spin qubits, Nature (London) **608**, 682 (2022).
[19] S. D. Liles, D. J. Halverson, Z. Wang, A. Shamim, R. S. Eggli, I. K. Jin, J. Hillier, K. Kumar, I. Vorreiter, M. J. Rendell, J. Y. Huang, C. C. Escott, F. E. Hudson, W. H. Lim, D. Culcer, A. S. Dzurak, and A. R. Hamilton, A singlet-triplet hole-spin qubit in MOS silicon, Nat. Commun. **15**, 7690 (2024).
[20] F. Borsoi, N. W. Hendrickx, V. John, M. Meyer, S. Motz, F. van Riggelen, A. Sammak, S. L. de Snoo, G. Scappucci, and M. Veldhorst, Shared control of a 16 semiconductor quantum dot crossbar array, Nat. Nanotechnol. **19**, 21 (2023).
[21] X. Xue, M. Russ, N. Samkharadze, B. Undseth, A. Sammak, G. Scappucci, and L. M. K. Vandersypen, Quantum logic with spin qubits crossing the surface code threshold, Nature (London) **601**, 343 (2022).
[22] A. R. Mills, C. R. Guinn, M. J. Gullans, A. J. Sigillito, M. M. Feldman, E. Nielsen, and J. R. Petta, Two-qubit silicon quantum processor with operation fidelity exceeding 99%, Sci. Adv. **8**, eabn5130 (2022).
[23] A. Noiri, K. Takeda, T. Nakajima, T. Kobayashi, A. Sammak, G. Scappucci, and S. Tarucha, Fast universal quantum gate above the fault-tolerance threshold in silicon, Nature (London) **601**, 338 (2022).
[24] W. I. L. Lawrie, M. Rimbach-Russ, F. v. Riggelen, N. W. Hendrickx, S. L. d. Snoo, A. Sammak, G. Scappucci, J. Helsen, and M. Veldhorst, Simultaneous single-qubit driving of semiconductor spin qubits at the fault-tolerant threshold, Nat. Commun. **14**, 3617 (2023).
[25] N. Hendrickx, D. Franke, A. Sammak, G. Scappucci, and M. Veldhorst, Fast two-qubit logic with holes in germanium, Nature (London) **577**, 487 (2020).
[26] S. Geyer, B. Hetényi, S. Bosco, L. C. Camenzind, R. S. Eggli, A. Fuhrer, D. Loss, R. J. Warburton, D. M. Zumbühl, and A. V. Kuhlmann, Anisotropic exchange interaction of two hole-spin qubits, Nat. Phys. **20**, 1152 (2024).
[27] C.-A. Wang, V. John, H. Tidjani, C. X. Yu, A. S. Ivlev, C. Déprez, F. van Riggelen-Doelman, B. D. Woods, N. W. Hendrickx, W. I. L. Lawrie, L. E. A. Stehouwer, S. D. Oosterhout, A. Sammak, M. Friesen, G. Scappucci, S. L. de Snoo, M. Rimbach-Russ, F. Borsoi, and M. Veldhorst, Operating semiconductor quantum processors with hopping spins, Science **385**, 447 (2024).
[28] M. J. Carballido, S. Svab, R. S. Eggli, T. Patlatiuk, P. Chevalier Kwon, J. Schuff, R. M. Kaiser, L. C. Camenzind, A. Li, N. Ares, E. P. A. M. Bakkers, S. Bosco, J. C. Egues, D. Loss, and D. M. Zumbühl, Compromise-free scaling of qubit speed and coherence, Nat. Commun. **16**, 7616 (2025).
[29] M. Bassi, E. A. Rodríguez-Mena, B. Brun, S. Zihlmann, T. Nguyen, V. Champain, J. C. Abadillo-Uriel, B. Bertrand, H. Niebojewski, R. Maurand, Y.-M. Niquet, X. Jehl, S. De Franceschi, and V. Schmitt, Optimal operation of hole spin qubits, Nat. Phys. **22**, 75 (2026).
[30] F. N. M. Froning, L. C. Camenzind, O. A. H. van der Molen, A. Li, E. P. A. M. Bakkers, D. M. Zumbühl, and F. R. Braakman, Ultrafast hole spin qubit with

gate-tunable spin–orbit switch functionality, Nat. Nanotechnol. **16**, 308 (2021).
[31] K. Wang, G. Xu, F. Gao, H. Liu, R.-L. Ma, X. Zhang, Z. Wang, G. Cao, T. Wang, J.-J. Zhang, D. Culcer, X. Hu, H.-W. Jiang, H.-O. Li, G.-C. Guo, and G.-P. Guo, Ultrafast coherent control of a hole spin qubit in a germanium quantum dot, Nat. Commun. **13**, 206 (2022).
[32] V. John, C. X. Yu, B. van Straaten, E. A. Rodríguez-Mena, M. Rodríguez, S. D. Oosterhout, L. E. A. Stehouwer, G. Scappucci, M. Rimbach-Russ, S. Bosco, F. Borsoi, Y.-M. Niquet, and M. Veldhorst, Robust and localised control of a 10-spin qubit array in germanium, Nat. Commun. **16**, 10560 (2025).
[33] S. G. J. Philips, M. T. Madzik, S. V. Amitonov, S. L. de Snoo, M. Russ, N. Kalhor, C. Volk, W. I. L. Lawrie, D. Brousse, L. Tryputen, B. P. Wuetz, A. Sammak, M. Veldhorst, G. Scappucci, and L. M. K. Vandersypen, Universal control of a six-qubit quantum processor in silicon, Nature (London) **609**, 919 (2022).
[34] N. W. Hendrickx, W. I. L. Lawrie, M. Russ, F. van Riggelen, S. L. de Snoo, R. N. Schouten, A. Sammak, G. Scappucci, and M. Veldhorst, A four-qubit germanium quantum processor, Nature (London) **591**, 580 (2021).
[35] X. Zhang, E. Morozova, M. Rimbach-Russ, D. Jirovec, T.-K. Hsiao, P. C. Fariña, C.-A. Wang, S. D. Oosterhout, A. Sammak, G. Scappucci, M. Veldhorst, and L. M. K. Vandersypen, Universal control of four singlet–triplet qubits, Nat. Nanotechnol. **20**, 209 (2025).
[36] F. Vigneau, F. Fedele, A. Chatterjee, D. Reilly, F. Kuemmeth, M. F. Gonzalez-Zalba, E. Laird, and N. Ares, Probing quantum devices with radio-frequency reflectometry, Appl. Phys. Rev. **10**, 021305 (2023).
[37] P. Harvey-Collard, B. D'Anjou, M. Rudolph, N. T. Jacobson, J. Dominguez, G. A. Ten Eyck, J. R. Wendt, T. Pluym, M. P. Lilly, W. A. Coish, M. Pioro-Ladrière, and M. S. Carroll, High-fidelity single-shot readout for a spin qubit via an enhanced latching mechanism, Phys. Rev. X **8**, 021046 (2018).
[38] G. A. Oakes, V. N. Ciriano-Tejel, D. F. Wise, M. A. Fogarty, T. Lundberg, C. Lainé, S. Schaal, F. Martins, D. J. Ibberson, L. Hutin, B. Bertrand, N. Stelmashenko, J. W. A. Robinson, L. Ibberson, A. Hashim, I. Siddiqi, A. Lee, M. Vinet, C. G. Smith, J. J. L. Morton, and M. F. Gonzalez-Zalba, Fast high-fidelity single-shot readout of spins in silicon using a single-electron box, Phys. Rev. X **13**, 011023 (2023).
[39] E. J. Connors, J. Nelson, and J. M. Nichol, Rapid high-fidelity spin-state readout in Si/Si-Ge quantum dots via rf reflectometry, Phys. Rev. Appl. **13**, 024019 (2020).
[40] G. Zheng, N. Samkharadze, M. L. Noordam, N. Kalhor, D. Brousse, A. Sammak, G. Scappucci, and L. M. K. Vandersypen, Rapid gate-based spin read-out in silicon using an on-chip resonator, Nat. Nanotechnol. **14**, 742 (2019).
[41] M. Urdampilleta, D. J. Niegemann, E. Chanrion, B. Jadot, C. Spence, P.-A. Mortemousque, C. Bäuerle, L. Hutin, B. Bertrand, S. Barraud, R. Maurand, M. Sanquer, X. Jehl, S. De Franceschi, M. Vinet, and T. Meunier, Gate-based high fidelity spin readout in a CMOS device, Nat. Nanotechnol. **14**, 737 (2019).
[42] R. Zhao, T. Tanttu, K. Y. Tan, B. Hensen, K. W. Chan, J. C. C. Hwang, R. C. C. Leon, C. H. Yang, W. Gilbert, F. E. Hudson, K. M. Itoh, A. A. Kiselev, T. D. Ladd, A. Morello, A. Laucht, and A. S. Dzurak, Single-spin qubits in isotopically enriched silicon at low magnetic field, Nat. Commun. **10**, 5500 (2019).
[43] N. M. Chtchelkatchev and Y. V. Nazarov, Andreev quantum dots for spin manipulation, Phys. Rev. Lett. **90**, 226806 (2003).
[44] S. Park and A. L. Yeyati, Andreev spin qubits in multichannel Rashba nanowires, Phys. Rev. B **96**, 125416 (2017).
[45] M. Hays, V. Fatemi, D. Bouman, J. Cerrillo, S. Diamond, K. Serniak, T. Connolly, P. Krogstrup, J. Nygård, A. L. Yeyati, A. Geresdi, and M. H. Devoret, Coherent manipulation of an Andreev spin qubit, Science **373**, 430 (2021).
[46] M. Hays, V. Fatemi, K. Serniak, D. Bouman, S. Diamond, G. de Lange, P. Krogstrup, J. Nygård, A. Geresdi, and M. H. Devoret, Continuous monitoring of a trapped superconducting spin, Nat. Phys. **16**, 1103 (2020).
[47] M. Pita-Vidal, A. Bargerbos, R. Žitko, L. J. Splitthoff, L. Grünhaupt, J. J. Wesdorp, Y. Liu, L. P. Kouwenhoven, R. Aguado, B. van Heck, A. Kou, and C. K. Andersen, Direct manipulation of a superconducting spin qubit strongly coupled to a transmon qubit, Nat. Phys. **19**, 1110 (2023).
[48] M. Pita-Vidal, J. J. Wesdorp, L. J. Splitthoff, A. Bargerbos, Y. Liu, L. P. Kouwenhoven, and C. K. Andersen, Strong tunable coupling between two distant superconducting spin qubits, Nat. Phys. **20**, 1158 (2024).
[49] A. Bargerbos, M. Pita-Vidal, R. Žitko, L. J. Splitthoff, L. Grünhaupt, J. J. Wesdorp, Y. Liu, L. P. Kouwenhoven, R. Aguado, C. K. Andersen, A. Kou, and B. van Heck, Spectroscopy of spin-split Andreev levels in a quantum dot with superconducting leads, Phys. Rev. Lett. **131**, 097001 (2023).
[50] A. Bargerbos, M. Pita-Vidal, R. Žitko, J. Á vila, L. J. Splitthoff, L. Grünhaupt, J. J. Wesdorp, C. K. Andersen, Y. Liu, L. P. Kouwenhoven, R. Aguado, A. Kou, and B. van Heck, Singlet-doublet transitions of a quantum dot Josephson junction detected in a transmon circuit, PRX Quantum **3**, 030311 (2022).
[51] L. Tosi, C. Metzger, M. F. Goffman, C. Urbina, H. Pothier, S. Park, A. L. Yeyati, J. Nygård, and P. Krogstrup, Spin-orbit splitting of Andreev states revealed by microwave spectroscopy, Phys. Rev. X **9**, 011010 (2019).
[52] H. Lu, D. F. Bofill, Z. Sun, T. Kanne, J. Nygård, M. Kjaergaard, and V. Fatemi, Andreev spin relaxation time in a shadow-evaporated InAs weak link, Phys. Rev. Appl. **24**, 024046 (2025).
[53] S. Hoffman, M. Hays, K. Serniak, T. Hazard, and C. Tahan, Decoherence in Andreev spin qubits, Phys. Rev. B **111**, 045304 (2025).
[54] L. Lakic, W. I. L. Lawrie, D. van Driel, L. E. A. Stehouwer, Y. Su, M. Veldhorst, G. Scappucci, F. Kuemmeth, and A. Chatterjee, A quantum dot in germanium proximitized by a superconductor, Nat. Mater. **24**, 552 (2025).
[55] M. Hinderling, S. C. ten Kate, M. Coraiola, D. Z. Haxell, M. Stiefel, M. Mergenthaler, S. Paredes, S. W. Bedell, D. Sabonis, and F. Nichele, Direct microwave spectroscopy

of Andreev bound states in planar Ge Josephson junctions, PRX Quantum **5**, 030357 (2024).
[56] C. Adelsberger, H. F. Legg, D. Loss, and J. Klinovaja, Microscopic analysis of proximity-induced superconductivity and metallization effects in superconductor-germanium hole nanowires, Phys. Rev. B **108**, 155433 (2023).
[57] S. S. Babkin, B. Joecker, K. Flensberg, M. Serbyn, and J. Danon, Superconducting proximity effect in two-dimensional hole gases, Phys. Rev. B **111**, 214518 (2025).
[58] P. D. Johannsen, H. F. Legg, S. Bosco, D. Loss, and J. Klinovaja, Atypical Josephson effect in hybrid superconductor-hole systems, Phys. Rev. Res. **8** 013289 (2026).
[59] D. M. Pino, R. S. Souto, M. J. Calderón, R. Aguado, and J. C. Abadillo-Uriel, Theory of superconducting proximity effect in hole-based hybrid semiconductor-superconductor devices, Phys. Rev. B **111**, 235443 (2025).
[60] M. Luethi, K. Laubscher, S. Bosco, D. Loss, and J. Klinovaja, Planar Josephson junctions in germanium: Effect of cubic spin-orbit interaction, Phys. Rev. B **107**, 035435 (2023).
[61] K. Laubscher, J. D. Sau, and S. Das Sarma, Majorana zero modes in gate-defined germanium hole nanowires, Phys. Rev. B **109**, 035433 (2024).
[62] A. Tosato, V. Levajac, J.-Y. Wang, C. J. Boor, F. Borsoi, M. Botifoll, C. N. Borja, S. Martí-Sánchez, J. Arbiol, A. Sammak, M. Veldhorst, and G. Scappucci, Hard superconducting gap in germanium, Commun. Mater. **4**, 23 (2023).
[63] K. Aggarwal, A. Hofmann, D. Jirovec, I. Prieto, A. Sammak, M. Botifoll, S. Martí-Sánchez, M. Veldhorst, J. Arbiol, G. Scappucci, J. Danon, and G. Katsaros, Enhancement of proximity-induced superconductivity in a planar Ge hole gas, Phys. Rev. Res. **3**, L022005 (2021).
[64] J. A. Steele, P. J. Strohbeen, C. Verdi, A. Baktash, A. Danilenko, Y.-H. Chen, J. van Dijk, F. H. Knudsen, A. Leblanc, D. Perconte, L. Wang, E. Demler, S. Salmani-Rezaie, P. Jacobson, and J. Shabani, Superconductivity in substitutional Ga-hyperdoped Ge epitaxial thin films, Nat. Nanotechnol. **20**, 1757 (2025).
[65] O. Sagi, A. Crippa, M. Valentini, M. Janik, L. Baghumyan, G. Fabris, L. Kapoor, F. Hassani, J. Fink, S. Calcaterra, D. Chrastina, G. Isella, and G. Katsaros, A gate tunable transmon qubit in planar Ge, Nat. Commun. **15**, 6400 (2024).
[66] E. Kiyooka, C. Tangchingchai, L. Noirot, A. Leblanc, B. Brun, S. Zihlmann, R. Maurand, V. Schmitt, É. Dumur, J.-M. Hartmann, F. Lefloch, and S. De Franceschi, Gatemon qubit on a germanium quantum-well heterostructure, Nano Lett. **25**, 562 (2025).
[67] O. Moutanabbir, S. Assali, A. Attiaoui, G. Daligou, P. Daoust, P. D. Vecchio, S. Koelling, L. Luo, and N. Rotaru, Nuclear spin-depleted, isotopically enriched ^{70}Ge/^{28}Si^{70}Ge quantum wells, Adv. Mater. **36**, 2305703 (2024).
[68] J. Fischer, W. A. Coish, D. V. Bulaev, and D. Loss, Spin decoherence of a heavy hole coupled to nuclear spins in a quantum dot, Phys. Rev. B **78**, 155329 (2008).
[69] S. Bosco and D. Loss, Fully tunable hyperfine interactions of hole spin qubits in Si and Ge quantum dots, Phys. Rev. Lett. **127**, 190501 (2021).
[70] P. Philippopoulos, S. Chesi, and W. A. Coish, First-principles hyperfine tensors for electrons and holes in GaAs and silicon, Phys. Rev. B **101**, 115302 (2020).
[71] D. Costa, P. D. Vecchio, K. Hudson, L. E. A. Stehouwer, A. Tosato, D. D. Esposti, V. Calvi, L. Moreschini, M. LodariS. Bosco, and G. Scappucci, Buried unstrained germanium channels: A lattice-matched platform for quantum technology, Adv. Sci. **13**, e00066.
[72] S. Bosco, M. Benito, C. Adelsberger, and D. Loss, Squeezed hole spin qubits in Ge quantum dots with ultrafast gates at low power, Phys. Rev. B **104**, 115425 (2021).
[73] L. Mauro, M. J. Rodríguez, E. A. Rodríguez-Mena, and Y.-M. Niquet, Hole spin qubits in unstrained germanium layers, npj Quantum Inf. **11**, 167 (2025).
[74] P. Del Vecchio, S. Bosco, D. Loss, and O. Moutanabbir, Fully tunable strong spin-orbit interactions in light hole germanium quantum channels, Commun. Phys. (2026).
[75] P. Del Vecchio and O. Moutanabbir, Light-hole gate-defined spin-orbit qubit, Phys. Rev. B **107**, L161406 (2023).
[76] P. Del Vecchio and O. Moutanabbir, Light-hole spin confined in germanium, Phys. Rev. B **110**, 045409 (2024).
[77] A. Leblanc, C. Tangchingchai, Z. Sadre Momtaz, E. Kiyooka, J.-M. Hartmann, F. Gustavo, J.-L. Thomassin, B. Brun, V. Schmitt, S. Zihlmann, R. Maurand, É. Dumur, S. De Franceschi, and F. Lefloch, Gate- and flux-tunable $\sin(2\varphi)$ Josephson element with planar-Ge junctions, Nat. Commun. **16**, 1010 (2025).
[78] M. Valentini, O. Sagi, L. Baghumyan, T. de Gijsel, J. Jung, S. Calcaterra, A. Ballabio, J. Aguilera Servin, K. Aggarwal, M. Janik, T. Adletzberger, R. Seoane Souto, M. Leijnse, J. Danon, C. Schrade, E. Bakkers, D. Chrastina, G. Isella, and G. Katsaros, Parity-conserving Cooper-pair transport and ideal superconducting diode in planar germanium, Nat. Commun. **15**, 169 (2024).
[79] M. Spethmann, S. Bosco, A. Hofmann, J. Klinovaja, and D. Loss, High-fidelity two-qubit gates of hybrid superconducting-semiconducting singlet-triplet qubits, Phys. Rev. B **109**, 085303 (2024).
[80] H.-S. Goan, G. J. Milburn, H. M. Wiseman, and H. Bi Sun, Continuous quantum measurement of two coupled quantum dots using a point contact: A quantum trajectory approach, Phys. Rev. B **63**, 125326 (2001).
[81] M. Boissonneault, J. M. Gambetta, and A. Blais, Dispersive regime of circuit QED: Photon-dependent qubit dephasing and relaxation rates, Phys. Rev. A **79**, 013819 (2009).
[82] D. Svastits, B. Hetényi, G. Széchenyi, J. Wootton, D. Loss, S. Bosco, and A. Pályi, Readout sweet spots for spin qubits with strong spin-orbit interaction, Phys. Rev. Lett. **136**, 117001 (2026).
[83] M. Pita-Vidal, J. J. Wesdorp, and C. K. Andersen, Blueprint for all-to-all-connected superconducting spin qubits, PRX Quantum **6**, 010308 (2025).
[84] H. Lu, I. A. Day, A. R. Akhmerov, B. van Heck, and V. Fatemi, Kramers-protected hardware-efficient error correction with Andreev spin qubits, Phys. Rev. Lett. **135**, 210602 (2025).
[85] L. M. K. Vandersypen, H. Bluhm, J. S. Clarke, A. S. Dzurak, R. Ishihara, A. Morello, D. J. Reilly,

L. R. Schreiber, and M. Veldhorst, Interfacing spin qubits in quantum dots and donors—hot, dense, and coherent, npj Quantum Inf. **3**, 34 (2017).

[86] W. G. van der Wiel, S. De Franceschi, J. M. Elzerman, T. Fujisawa, S. Tarucha, and L. P. Kouwenhoven, Electron transport through double quantum dots, Rev. Mod. Phys. **75**, 1 (2002).

[87] J. C. Abadillo-Uriel, E. A. Rodríguez-Mena, B. Martinez, and Y.-M. Niquet, Hole-spin driving by strain-induced spin-orbit interactions, Phys. Rev. Lett. **131**, 097002 (2023).

[88] C.-A. Wang, H. E. Ercan, M. F. Gyure, G. Scappucci, M. Veldhorst, and M. Rimbach-Russ, Modeling of planar germanium hole qubits in electric and magnetic fields, npj Quantum Inf. **10**, 102 (2024).

[89] M. Rimbach-Russ, V. John, B. van Straaten, and S. Bosco, Gapless single-spin qubit, Phys. Rev. Lett. **135**, 197001 (2025).

[90] L. A. Terrazos, E. Marcellina, Z. Wang, S. N. Coppersmith, M. Friesen, A. R. Hamilton, X. Hu, B. Koiller, A. L. Saraiva, D. Culcer, and R. B. Capaz, Theory of hole-spin qubits in strained germanium quantum dots, Phys. Rev. B **103**, 125201 (2021).

[91] R. Seoane Souto and R. Aguado, Subgap states in semiconductor-superconductor devices for quantum technologies: Andreev qubits and minimal majorana chains, in *New Trends and Platforms for Quantum Technologies*, Eds. R. Aguado, R. Citro, M. Lewenstein, and M. Stern (Springer Nature Switzerland, Cham, 2024), p. 223.

[92] M. Žonda, P. Zalom, T. c. v. Novotný, G. Loukeris, J. Bätge, and V. Pokorný, Generalized atomic limit of a double quantum dot coupled to superconducting leads, Phys. Rev. B **107**, 115407 (2023).

[93] E. Vecino, A. Martín-Rodero, and A. L. Yeyati, Josephson current through a correlated quantum level: Andreev states and π junction behavior, Phys. Rev. B **68**, 035105 (2003).

[94] P. Zalom, K. Wrześniewski, T. c. v. Novotný, and I. Weymann, Double quantum dot Andreev molecules: Phase diagrams and critical evaluation of effective models, Phys. Rev. B **110**, 134506 (2024).

[95] A. Blais, A. L. Grimsmo, S. M. Girvin, and A. Wallraff, Circuit quantum electrodynamics, Rev. Mod. Phys. **93**, 025005 (2021).

[96] J. Dijkema, X. Xue, P. Harvey-Collard, M. Rimbach-Russ, S. L. de Snoo, G. Zheng, A. Sammak, G. Scappucci, and L. M. K. Vandersypen, Cavity-mediated iSWAP oscillations between distant spins, Nat. Phys. **21**, 168 (2025).

[97] C. X. Yu, S. Zihlmann, J. C. Abadillo-Uriel, V. P. Michal, N. Rambal, H. Niebojewski, T. Bedecarrats, M. Vinet, É. Dumur, M. Filippone, B. Bertrand, S. De Franceschi, Y.-M. Niquet, and R. Maurand, Strong coupling between a photon and a hole spin in silicon, Nat. Nanotechnol. **18**, 741 (2023).

[98] F. De Palma, F. Oppliger, W. Jang, S. Bosco, M. Janík, S. Calcaterra, G. Katsaros, G. Isella, D. Loss, and P. Scarlino, Strong hole-photon coupling in planar Ge for probing charge degree and strongly correlated states, Nat. Commun. **15**, 10177 (2024).

[99] M. Janík, K. Roux, C. Borja-Espinosa, O. Sagi, A. Baghdadi, T. Adletzberger, S. Calcaterra, M. Botifoll, A. Garzón Manjón, J. Arbiol, D. Chrastina, G. Isella, I. M. Pop, and G. Katsaros, Strong charge-photon coupling in planar germanium enabled by granular aluminium superinductors, Nat. Commun. **16**, 2103 (2025).

[100] A. J. Landig, J. V. Koski, P. Scarlino, U. C. Mendes, A. Blais, C. Reichl, W. Wegscheider, A. Wallraff, K. Ensslin, and T. Ihn, Coherent spin–photon coupling using a resonant exchange qubit, Nature (London) **560**, 179 (2018).

[101] X. Mi, M. Benito, S. Putz, D. M. Zajac, J. M. Taylor, G. Burkard, and J. R. Petta, A coherent spin–photon interface in silicon, Nature (London) **555**, 599 (2018).

[102] S. Bosco, P. Scarlino, J. Klinovaja, and D. Loss, Fully tunable longitudinal spin-photon interactions in Si and Ge quantum dots, Phys. Rev. Lett. **129**, 066801 (2022).

[103] M. Benito, X. Mi, J. M. Taylor, J. R. Petta, and G. Burkard, Input-output theory for spin-photon coupling in Si double quantum dots, Phys. Rev. B **96**, 235434 (2017).

[104] P. Harvey-Collard, J. Dijkema, G. Zheng, A. Sammak, G. Scappucci, and L. M. K. Vandersypen, Coherent spin-spin coupling mediated by virtual microwave photons, Phys. Rev. X **12**, 021026 (2022).

[105] F. van Riggelen-Doelman, C.-A. Wang, S. L. de Snoo, W. I. L. Lawrie, N. W. Hendrickx, M. Rimbach-Russ, A. Sammak, G. Scappucci, C. Déprez, and M. Veldhorst, Coherent spin qubit shuttling through germanium quantum dots, Nat. Commun. **15**, 5716 (2024).

[106] X. Croot, X. Mi, S. Putz, M. Benito, F. Borjans, G. Burkard, and J. R. Petta, Flopping-mode electric dipole spin resonance, Phys. Rev. Res. **2**, 012006 (2020).

[107] P. M. Mutter and G. Burkard, Natural heavy-hole flopping mode qubit in germanium, Phys. Rev. Res. **3**, 013194 (2021).

[108] A. Sen, G. Frank, B. Kolok, J. Danon, and A. Pályi, Classification and magic magnetic field directions for spin-orbit-coupled double quantum dots, Phys. Rev. B **108**, 245406 (2023).

[109] J. Saez-Mollejo, D. Jirovec, Y. Schell, J. Kukucka, S. Calcaterra, D. Chrastina, G. Isella, M. Rimbach-Russ, S. Bosco, and G. Katsaros, Exchange anisotropies in microwave-driven singlet-triplet qubits, Nat. Commun. **16**, 3862 (2025).

[110] N. Didier, J. Bourassa, and A. Blais, Fast quantum nondemolition readout by parametric modulation of longitudinal qubit-oscillator interaction, Phys. Rev. Lett. **115**, 203601 (2015).

[111] J. Gambetta, A. Blais, M. Boissonneault, A. A. Houck, D. I. Schuster, and S. M. Girvin, Quantum trajectory approach to circuit QED: Quantum jumps and the Zeno effect, Phys. Rev. A **77**, 012112 (2008).

[112] A. A. Clerk, M. H. Devoret, S. M. Girvin, F. Marquardt, and R. J. Schoelkopf, Introduction to quantum noise, measurement, and amplification, Rev. Mod. Phys. **82**, 1155 (2010).

[113] T. Walter, P. Kurpiers, S. Gasparinetti, P. Magnard, A. Potočnik, Y. Salathé, M. Pechal, M. Mondal, M. Oppliger, C. Eichler, and A. Wallraff, Rapid high-fidelity single-shot dispersive readout of superconducting qubits, Phys. Rev. Appl. **7**, 054020 (2017).

[114] J. Hu, A. L. Manesco, A. Melo, T. V. Stefanski, C. K. Andersen, and V. Fatemi, Mixed spin-boson coupling for

qubit readout with suppressed residual shot-noise dephasing, arXiv:2503.13411.

[115] E. Jeffrey, D. Sank, J. Y. Mutus, T. C. White, J. Kelly, R. Barends, Y. Chen, Z. Chen, B. Chiaro, A. Dunsworth, A. Megrant, P. J. J. O'Malley, C. Neill, P. Roushan, A. Vainsencher, J. Wenner, A. N. Cleland, and J. M. Martinis, Fast accurate state measurement with superconducting qubits, Phys. Rev. Lett. **112**, 190504 (2014).

[116] D. T. McClure, H. Paik, L. S. Bishop, M. Steffen, J. M. Chow, and J. M. Gambetta, Rapid driven reset of a qubit readout resonator, Phys. Rev. Appl. **5**, 011001 (2016).

[117] C. C. Bultink, M. A. Rol, T. E. O'Brien, X. Fu, B. C. S. Dikken, C. Dickel, R. F. L. Vermeulen, J. C. de Sterke, A. Bruno, R. N. Schouten, and L. DiCarlo, Active resonator reset in the nonlinear dispersive regime of circuit QED, Phys. Rev. Appl. **6**, 034008 (2016).

[118] P. D. Kurilovich, T. Connolly, C. G. Bøttcher, D. K. Weiss, S. Hazra, V. R. Joshi, A. Z. Ding, H. Nho, S. Diamond, V. D. Kurilovich *et al.*, High-frequency readout free from transmon multi-excitation resonances, arXiv:2501.09161.

[119] T. Connolly, P. D. Kurilovich, V. D. Kurilovich, C. G. Bøttcher, S. Hazra, W. Dai, A. Z. Ding, V. R. Joshi, H. Nho, S. Diamond *et al.*, Full characterization of measurement-induced transitions of a superconducting qubit, arXiv:2506.05306.

[120] B. Harpt, J. Corrigan, N. Holman, P. Marciniec, D. Rosenberg, D. Yost, R. Das, R. Ruskov, C. Tahan, W. D. Oliver, R. McDermott, M. Friesen, and M. A. Eriksson, Ultra-dispersive resonator readout of a quantum-dot qubit using longitudinal coupling, npj Quantum Inf. **11**, 5 (2025).

[121] S. Bosco and M. Rimbach-Russ, Exchange-only spin-orbit qubits in silicon and germanium, Phys. Rev. Appl. **25**, L021002 (2026).

[122] Y. P. Kandel, H. Qiao, S. Fallahi, G. C. Gardner, M. J. Manfra, and J. M. Nichol, Coherent spin-state transfer via Heisenberg exchange, Nature (London) **573**, 553 (2019).

[123] M. T. P. Nguyen, M. Rimbach-Russ, L. M. K. Vandersypen, and S. Bosco, Single-step high-fidelity three-qubit gates by anisotropic chiral interactions, PRX Quantum **6**, 030326 (2025).

[124] D. Jirovec, P. M. Mutter, A. Hofmann, A. Crippa, M. Rychetsky, D. L. Craig, J. Kukucka, F. Martins, A. Ballabio, N. Ares, D. Chrastina, G. Isella, G. Burkard, and G. Katsaros, Dynamics of hole singlet-triplet qubits with large g-factor differences, Phys. Rev. Lett. **128**, 126803 (2022).

[125] 10.5281/zenodo.16024696.

[126] C.-F. Kam and X. Hu, Fast and high-fidelity dispersive readout of a spin qubit with squeezed microwave and resonator nonlinearity, npj Quantum Inf. **10**, 133 (2024)